Supporting Information for

Regulating interfacial reaction through electrolyte chemistry enables anion-rich interphase for wide-temperature zinc metal batteries

Yimei Chen, Kaijie Zhang, Zhixiao Xu, Facheng Gong, Renfei Feng, Zhehui Jin, Xiaolei Wang*

Table of Contents

1. Experimental Details

1.1 Material and Methods

Materials: Zinc sulfate heptahydrate ($ZnSO_4 \cdot 7H_2O$), zinc trifluoromethanesulfonate ($Zn(CF_3SO_3)_2$), zinc perchlorate hexahydrate ($Zn(ClO_4)_2 \, 6H_2O$), iodine (I_2), dimethylformamide (DMF), and polyvinylidene difluoride (PVDF), zinc acetate dihydrate ($Zn(OAc)_2 \cdot 2 \, H_2O$) were purchased from Thermo Fisher Scientific. Zinc chloride ($ZnCl_2$), alginic acid sodium salt, and oxalic acid ($H_2C_2O_4$) were purchased from Sigma-Aldrich. Commercial activated carbon (AC, TF-B520) was purchased from MTI Corporation. Ammonium metavanadate (NH_4VO_3) was purchased from Acros Organics. The separator (Whatman® glass microfiber filters, Grade GF/A, CAT No:1820-110) was purchased from Sigma-Aldrich. All the chemicals are in analytic grade and used without further purification.

Electrolyte Preparation: $ZnSO_4 \cdot 7H_2O$, $Zn(CF_3SO_3)_2$, $Zn(ClO_4)_2 \cdot 6H_2O$, $ZnCl_2$ was dissolved in deionized water to prepare 3.0 M electrolytes denoted as 3.0 M ZSO, 3.0 M Zn ($CF_3SO_3)_2$, 3.0 M ZClO (also referred as designed electrolyte or designed system) and 3.0 M $ZnCl_2$, respectively. Different concentrations (0.1 M, 0.3 M, 0.5 M) of $Zn(OAc)_2$ were added to 3.0 M ZClO electrolyte to make the OAc^--containing electrolyte, denoted as 3 M ZClO-x M $Zn(OAc)_2$ (x represents concentration). 10 mM I_3^- electrolytes were prepared by adding 10 mM I_2 into 0.1 M NaI solutions.

Electrode preparation: The Zn foil (100 μm, unless otherwise stated) was punched into discs with an area of 1.13 cm^{-2} and washed with ethanol. The I_2/AC cathode was prepared according to the previous paper [1]. Typically, the areal mass loading of I_2/AC was maintained at around 4-5 mg cm^{-2}. Vanadium oxide (VO_2) was synthesized through a hydrothermal reaction [2]. Specifically, 5.48 mmol of NH_4VO_3 and 9.2 mmol of $H_2C_2O_4$ were dissolved in 80 mL of deionized water and agitated for 40 minutes under ambient conditions. The resultant solution was subsequently transferred into a Teflon-lined autoclave and subjected to heating at 180 °C for a duration of 3 hours. Following the cooling process to room temperature, the precipitate obtained underwent a thorough washing procedure with deionized water, conducted at least thrice. The precipitate was then collected utilizing a centrifuge and subsequently subjected to vacuum drying at 60 °C overnight. The as-prepared VO_2 was further subjected to annealing at 300 °C for a duration of 3 hours in an argon (Ar) atmosphere. The synthesized VO_2 was mixed

with super P and PVDF in a mass ratio of 7:2:1, and the resulting slurry was coated on carbon cloth and dried under infrared light. The mass loading of V_2O_5 is 2.0-2.5 mg cm^{-2}. For the pouch cells, the mass loading of I_2/AC was controlled at around 3 mg cm^{-2}, and the separator and zinc foil were cut into 3.1*3.1 cm^2 square.

Electrochemical test: The electrochemical evaluation of the battery in this study was carried out using a Neware battery test system (CT-4008T-5V20mA-164, CT-4008T-5V50mA-164, CT-4008T-5V6A-S1, Shenzhen, China) within coin cells (CR-2032) or self-made pouch cells. The half-cell's rate capability and long-term cycling performance were assessed in a Zn//Zn symmetric cell employing 60 μL of electrolyte and Coulombic efficiency measurements were performed in a Zn//Cu asymmetrical battery with a cut-off voltage of 1.0 V. The Tafel plot was generated in a three-electrode system, utilizing a graphite electrode and saturated calomel electrode (SCE) as the counter and reference electrodes, respectively. Cyclic voltammetry (CV) and electrochemical impedance spectra (EIS) were conducted on an electrochemical workstation (VMP3, Biologic). The full cell configuration involved assembling a Zn anode and cathode materials, either I_2/AC or VO_2, separated by glass fiber and supplemented with 80 μL of electrolyte. The pouch cell was assembled with a 3 × 3 cm^2 zinc anode and an I_2/AC cathode, separated by glass fiber and supplemented with 300 μL of electrolyte. These components were sealed in a custom-made plastic cover. The Zn‖I_2/AC full cell's performance was assessed within a voltage window of 0.2-1.7 V, while the Zn‖VO_2 cell operated within a voltage range of 0.3-1.6 V.

Characterization: The crystalline structure of the electrodes was characterized by X-ray diffraction (XRD) conducted on an Ultima IV (Rigaku) diffractometer equipped with a Cu Kα X-ray source. The ex-situ small angle diffraction is conducted on Bruker D8D PLUS XRD. The morphologies of the electrode were scanned by scanning electron spectroscopy (SEM, Zeiss EVO M10), filed emission scanning electron spectroscopy (FESEM, Zeiss Sigma) equipped with energy dispersive x-ray analysis (EDX, Oxford). Fourier transform infrared (FTIR) mapping was performed on Nicolet 8700 infrared spectroscopy instrument with the KBr pellet technique. Raman spectroscopy and in-situ Raman were collected on a laser confocal Raman spectrometer (Renishaw in Via Qontor) with a laser wavelength of 532nm. ^{1}H Nuclear magnetic resonance spectrum (NMR, 600 MHz, D_2O) was tested on a Bruker AVANCE III spectrometer

(400 MHz). The surface wettability of the electrolyte was measured by a contact angle measuring system (Dataphysics OCA50). The synchrotron two-dimensional grazing-incidence X-ray diffraction (2D GIXRD) measurements were conducted at the VESPERS beamline of the Canadian Light Source (CLS). The zinc anode, cycled for different times, was taken out from the coin cell and washed with DI water and ethanol. The experimental setup utilized a beam size of approximately 3×6 μm, with incident angles set at 0.6°. The X-ray beam's energy for GIXRD analysis was 9.0755 keV. The data was analyzed using XMAS. The X-ray absorption spectra (XAS), encompassing both X-ray absorption near-edge structure (XANES) and extended X-ray absorption fine structure (EXAFS) of the samples at the Zn K-edge (9659 eV), were also gathered at the CLS. The Zn K-edge XANES data were recorded in transmission mode, with Zn foil as reference materials. The obtained EXAFS data were subsequently extracted and processed using the ATHENA software [3]. WT-EXAFS was analyzed via Fortran [4].

1.2 Theory/calculation

Density function theory (DFT) simulations: DFT simulations were conducted Gaussian 16 package to calculate the solvation energy and the desolvation barrier [5]. B3LYP with the 6-311G (2d 2p) basic set with a hybrid density functional method, has been applied to optimize the geometries of these structures and calculate the binding energies. Gaussview 6.0 was used for model building and result post-processing. The binding energy can be calculated by Equation (1),

$$E_{binding} = E(AB) - E(A) - E(B) \tag{1}$$

Here AB represents the total energy after the binding between Zn^{2+} and other species. A and B are the energy of a single Zn^{2+} and individual species exist in the electrolyte, respectively.

Molecular dynamics (MD) simulations: The MD simulations were performed through the GROMACS package with a gormos54a7 force field [6]. All simulations were carried out in a periodic cubic box with lengths of 5 nm. Systems were first minimized by the steepest descent method to limit the maximum force within 1000.0 kJ/(mol·nm). For each system, an MD run of 100 ps was carried out under canonical ensemble (NVT), followed by an MD run under isobaric–isothermal ensemble (NPT) for at least 5 ns until the system volume reached a constant value. The temperature of 300K and the pressure of 1.0 bar were controlled by the Berendsen

algorithm with a coupling constant of 0.2 and 1.0 ps, respectively. After that, NPT production of 50 ns at 300 K and 1.0 bar was performed using the Nose–Hoover thermostat with a 1.0 ps coupling constant and Parrinello–Rahman barostat with a 2.0 ps coupling constant [7]. Van der Waals, Coulomb, and neighbor list cutoff distances were taken to 1.0 nm. The long-range electrostatic interactions were treated by the PME method. All bonds were constrained using the LINCS algorithm. The MD simulations of various electrolyte systems over a temperature range of 273 K to 293 K at 1 atm were calculated for 100 ns to ensure the system reached equilibrium, with the final 10 ns of the simulation utilized for subsequent analysis, considering the system to be in an equilibrium state during this period. The assessment of hydrogen bonds (HB) involved a geometric criterion where the distance between two oxygen atoms (O) was stipulated to be <3.5 Å, and the angle of O–H···O was required to be <30° for the determination of hydrogen bonding interactions. Mean square displacement (MSD) analysis quantifies the average of the squared particle displacement over a given time interval t $(MSD(t)=|r(t)-r(0)|^2$. The self-diffusion coefficient D of water molecules was determined using the Einstein equation [8].

$$D = \lim_{t \to \infty} \frac{MSD(t)}{t} \qquad (2)$$

2. Supporting Figures
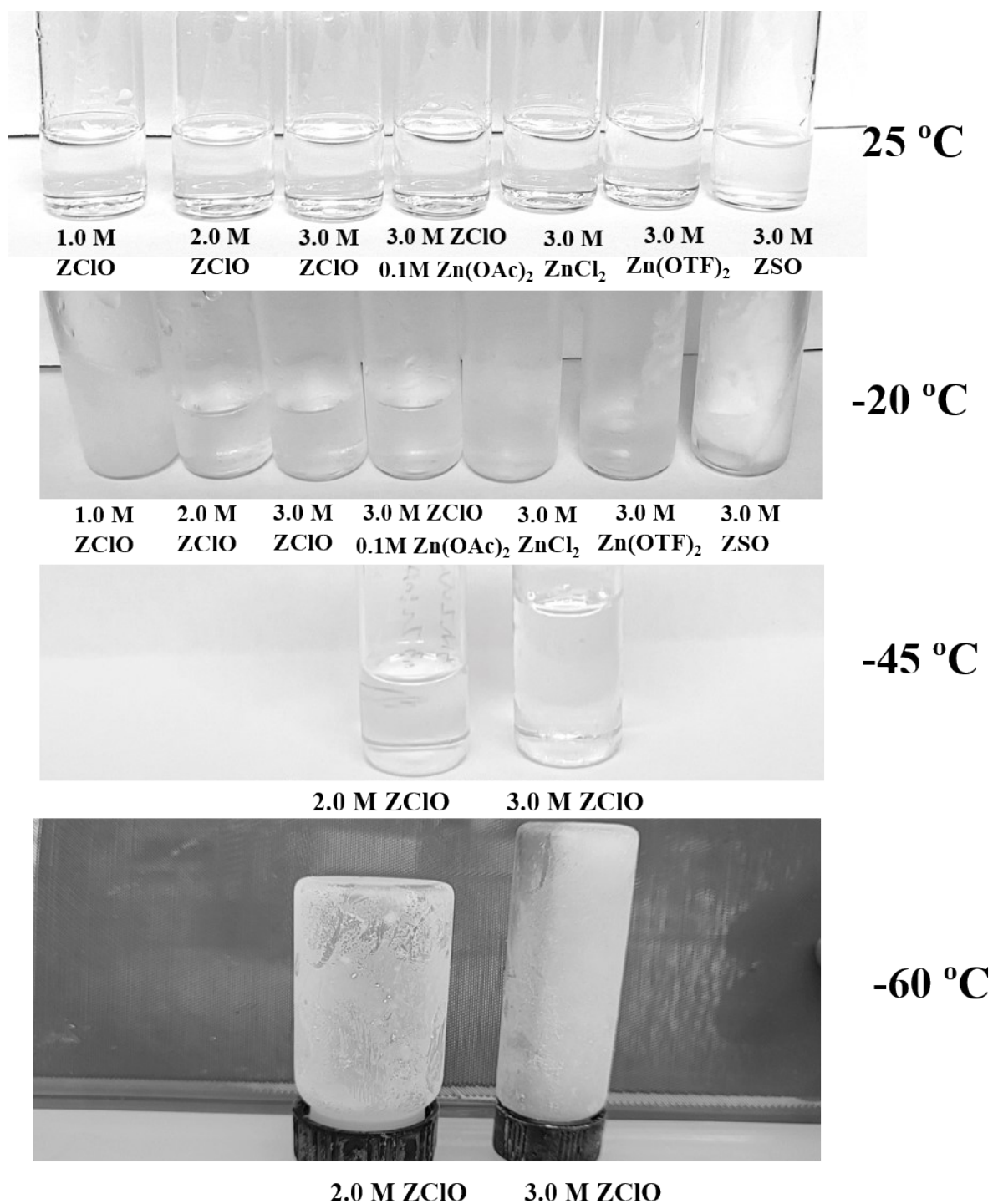
Figure S1. State of various electrolytes at various temperatures.

At –20 ºC, the 3.0 M ZSO solution solidified, whereas both 1.0 M ZClO, 3.0 M ZnCl$_2$, and 3.0 M Zn(CF$_3$SO$_3$)$_2$ exhibited a liquid-solid two-phase state. In contrast, 2.0 M and 3.0 M ZClO solutions maintain a transparent liquid state. Even down to -45 ºC, both 2 M and 3 M ZClO remain liquid, and at –60 ºC, both 2 M and 3 M ZClO electrolytes freeze.
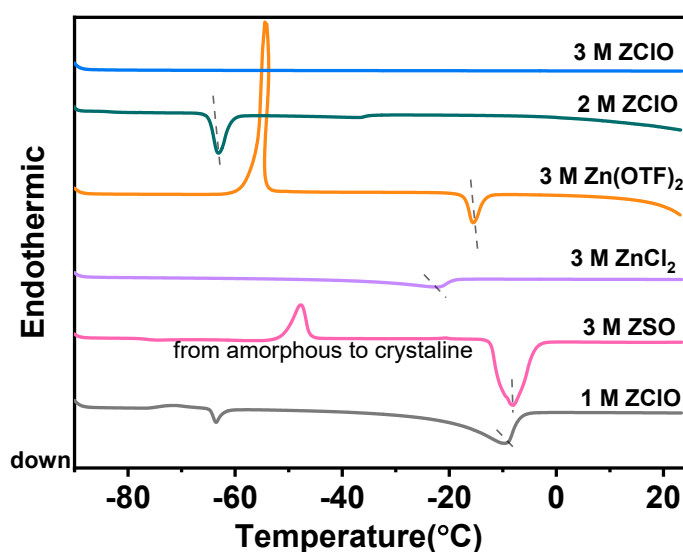
Figure S2. DSC curve of various electrolytes

Figure 1(a) illustrates the crystallization process from 25 °C to -90 °C, with a temperature ramp of 5 °C /min. The exothermic curves presented in this figure represent the crystallization temperature. Similarly, Figure S2 depicts the melting process from -90 °C to 25 °C using the same 5 °C /min ramp, with the endothermic curves indicating the melting temperature. The crystallization temperature is lower than the melting temperature. For 3 M ZSO solution exhibits a melting temperature of -8 °C, while its crystallization temperature drops to -36 °C.
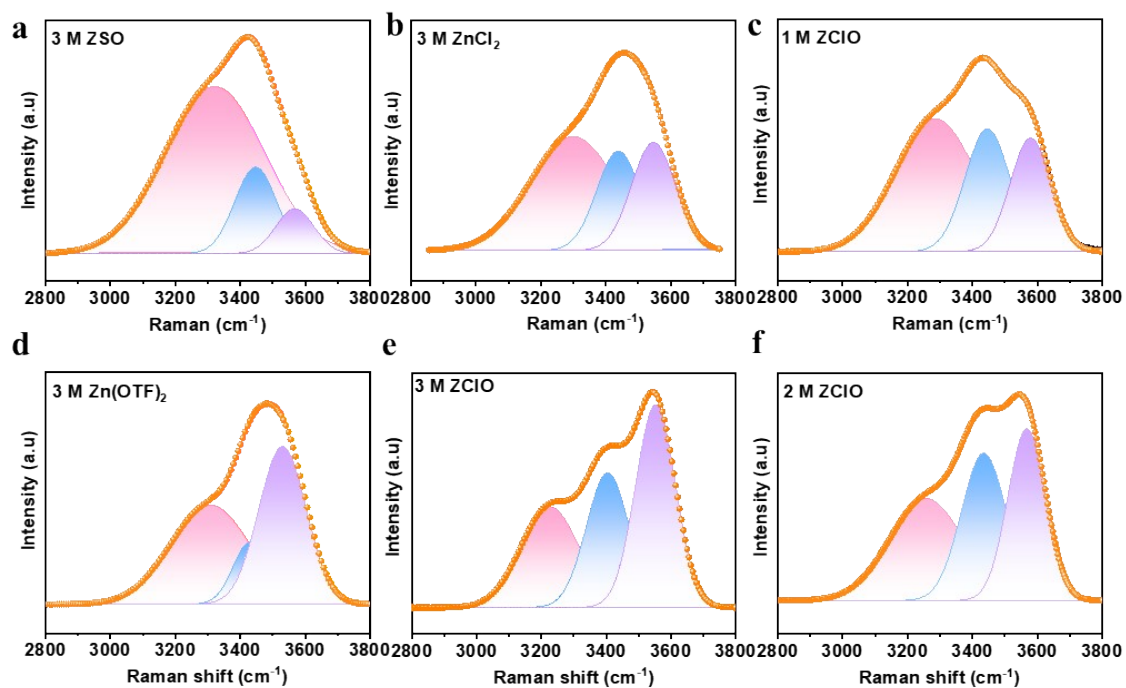
Figure S3. Raman spectrums of different electrolytes.
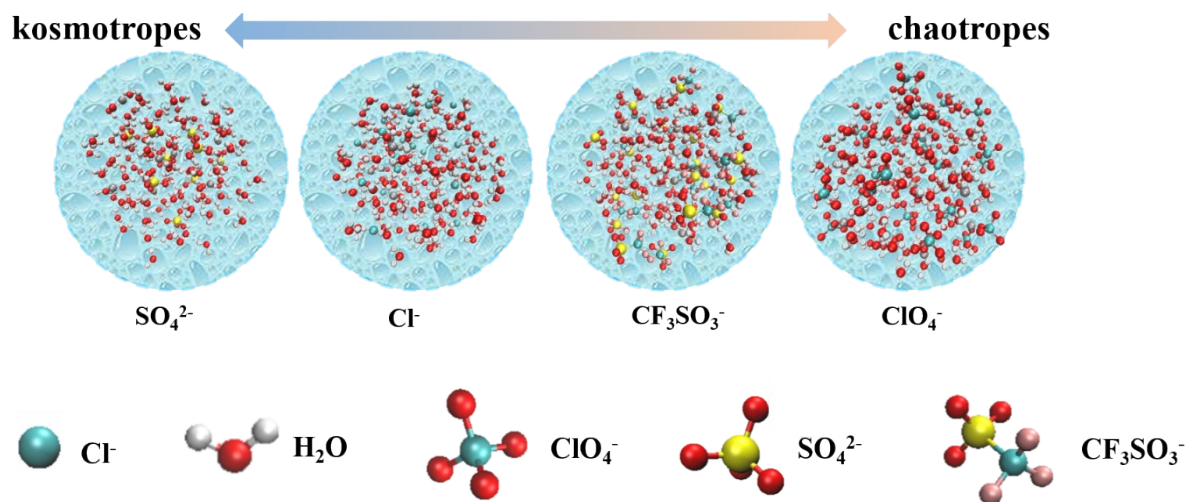
Figure S4. Hofmeister series of various anions.
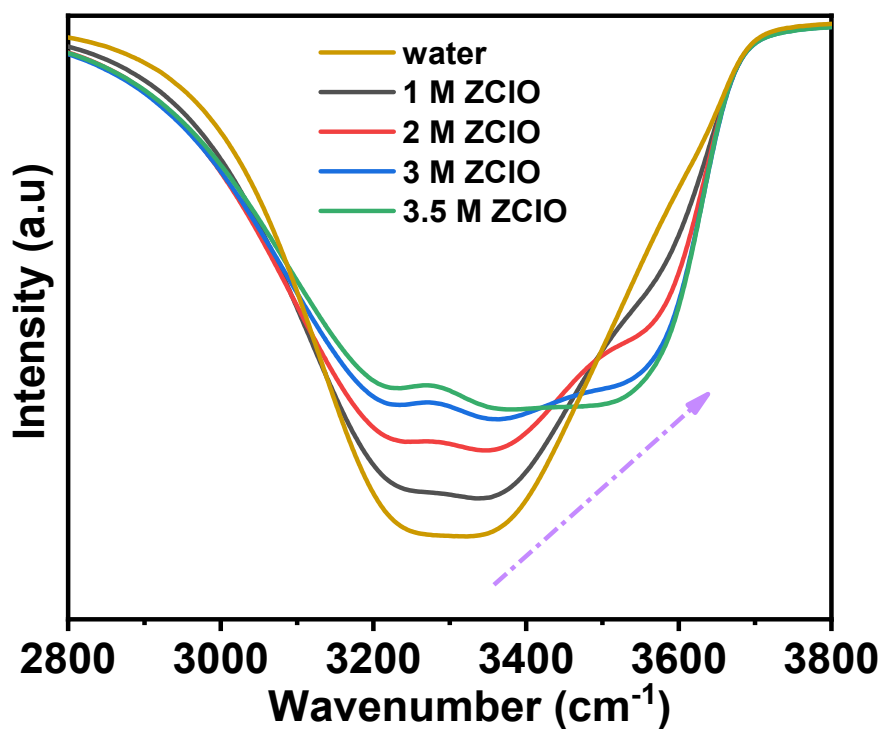
Figure S5. FTIR of ZClO with various concentrations.

Increasing the ZClO concentration induces a noticeable blue shift and a weakened peak intensity of O-H vibrations at 3250 and 3400 cm^{-1}, and the peak at 3550 cm^{-1} which corresponds to a weak or no HBs becomes pronounced at higher ZClO concentrations of 3.0 M, and 3.5 M (As 4.0 M cannot fully dissolve in water, 3.5 M is chosen as the maximum concentration), revealing the destruction of the hydrogen-bonded among water molecules and the formation of ClO_4^--H_2O HBs.
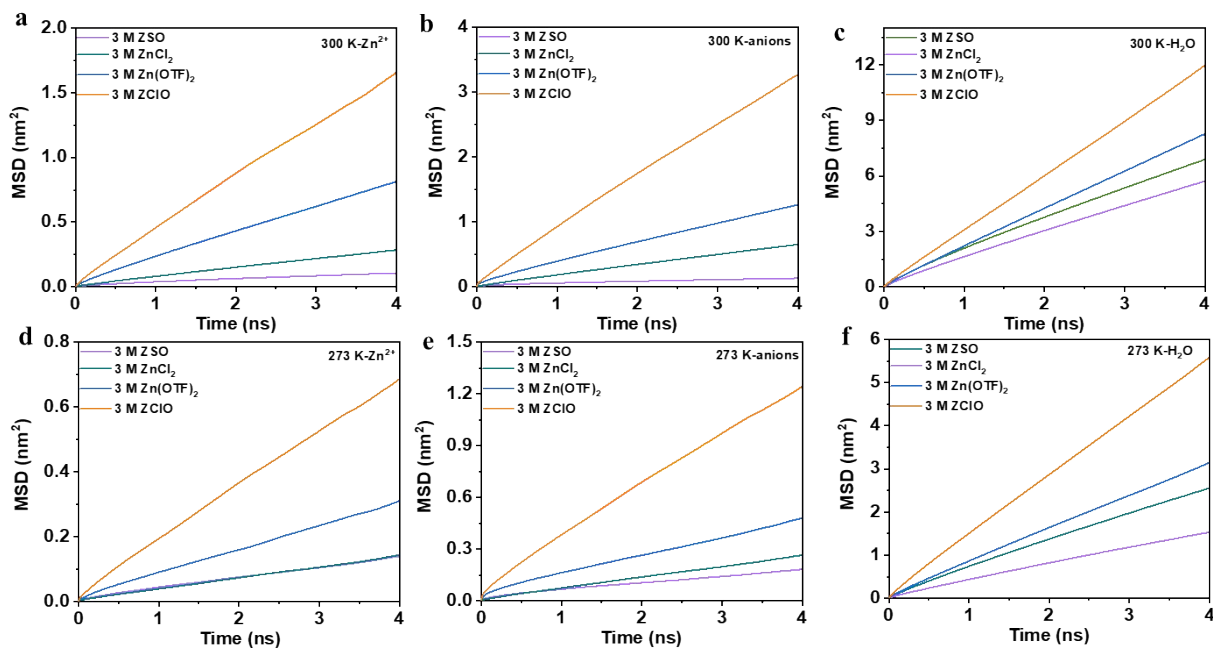
Figure S6. MSD of ClO_4^-, Zn^{2+}, and H_2O in various electrolytes at 300 K and 273 K.
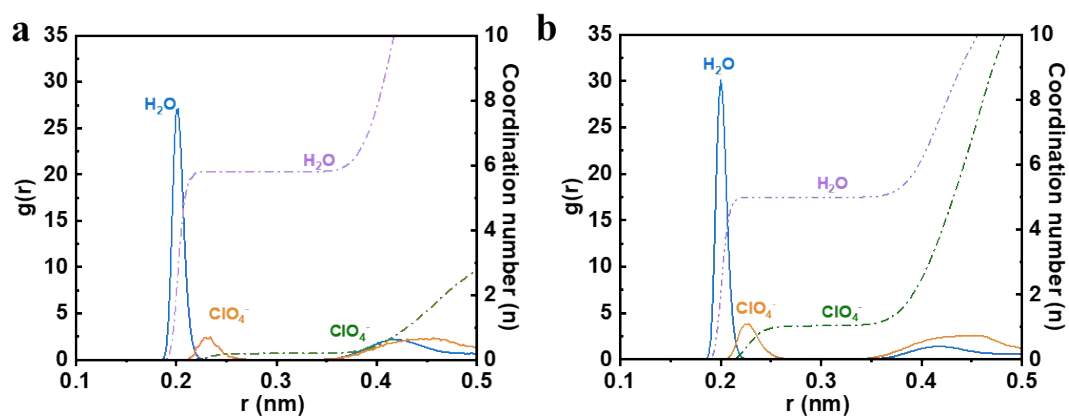
Figure S7. The coordination environment of Zn^{2+} in 1.0 M and 3.5 M ZClO electrolyte.
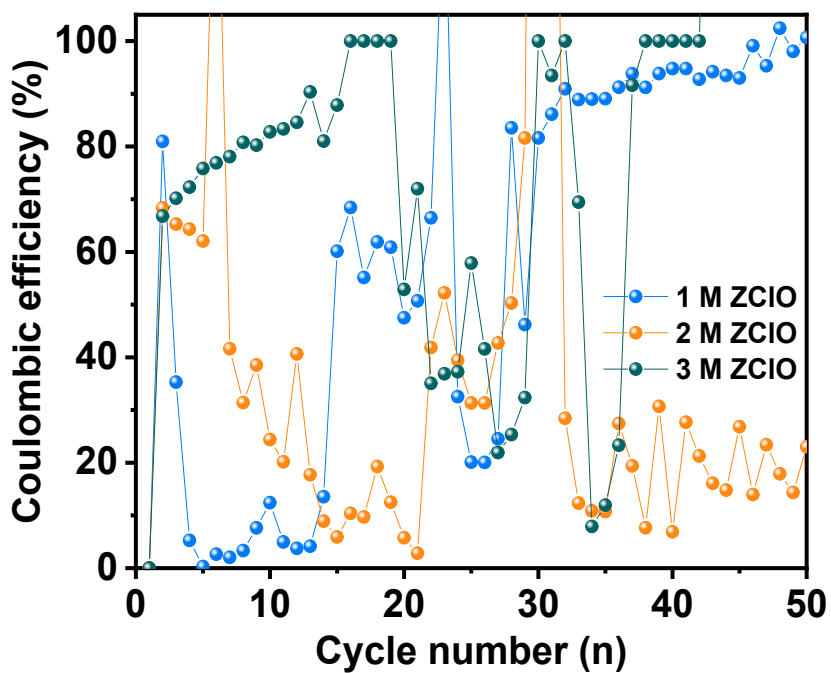
Figure S8. Coulombic efficiency of pure ZClO electrolytes.
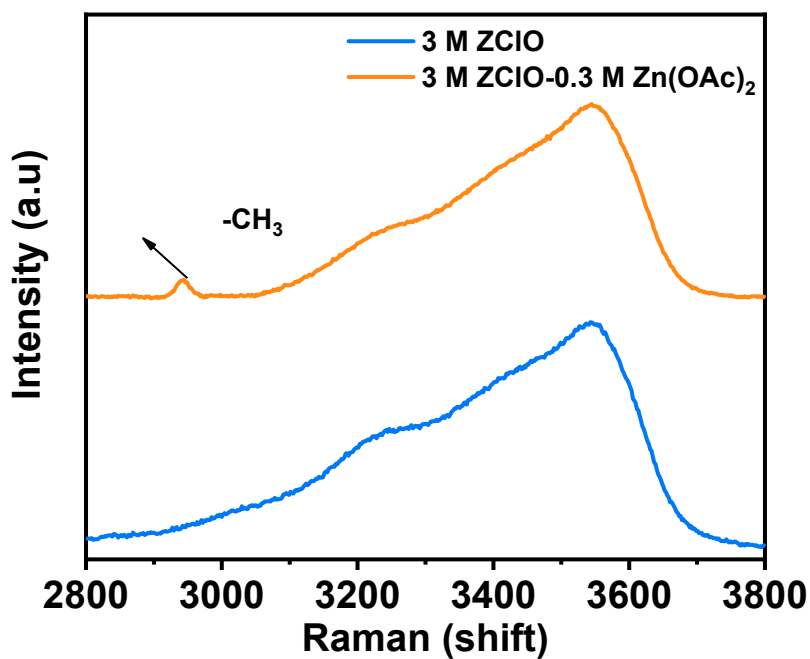
Figure S9. Raman results of different electrolytes.

The Raman spectra of the designed electrolyte show a peak at 2945 cm^{-1}, attributed to the symmetric vibrations of -CH$_3$ from OAc$^-$ group.
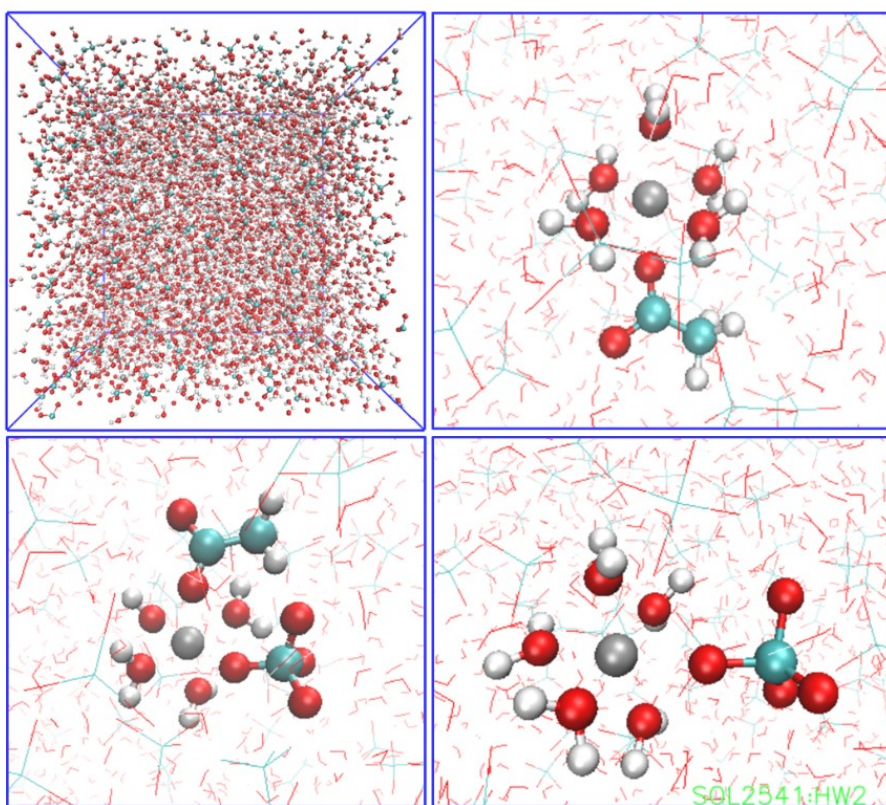
Figure S10. Co-existing solvation structures in the designed system.
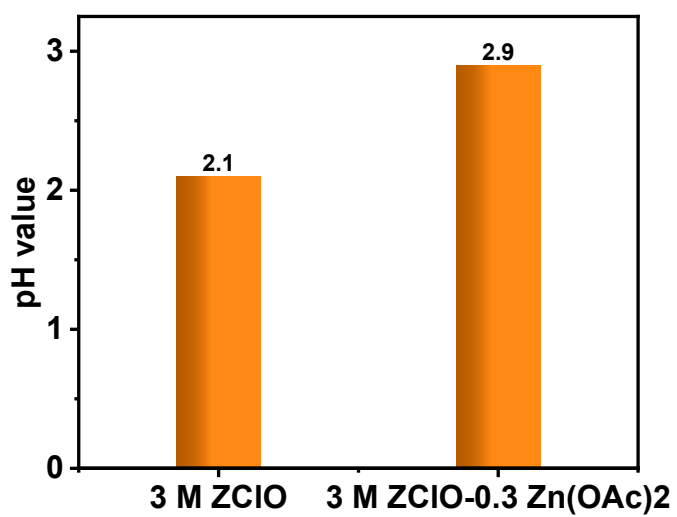
Figure S11. pH value of the electrolyte with and without 0.3 M Zn(OAc)$_2$ additive.
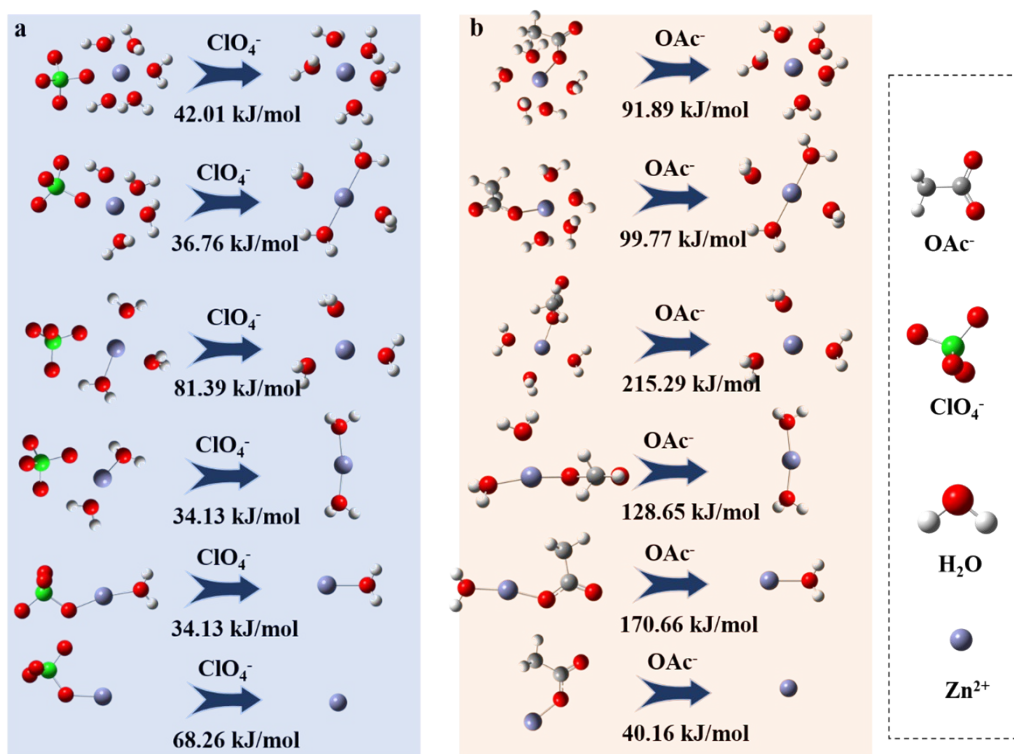
Figure S12. Diagram of the energy barriers in the step-by-step desolvation process (a 3.0 M ZClO, b 3.0 M ZClO+0.3 M Zn (OAc)$_2$).
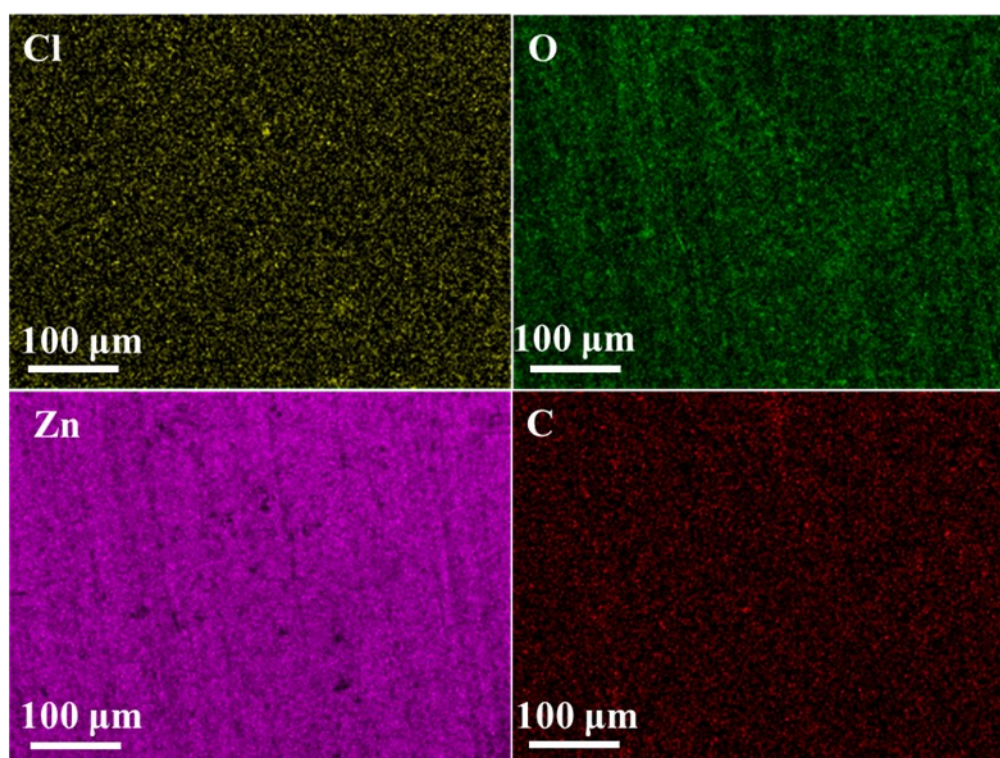
Figure S13. EDX mapping results of cycled Zn in the designed electrolyte.
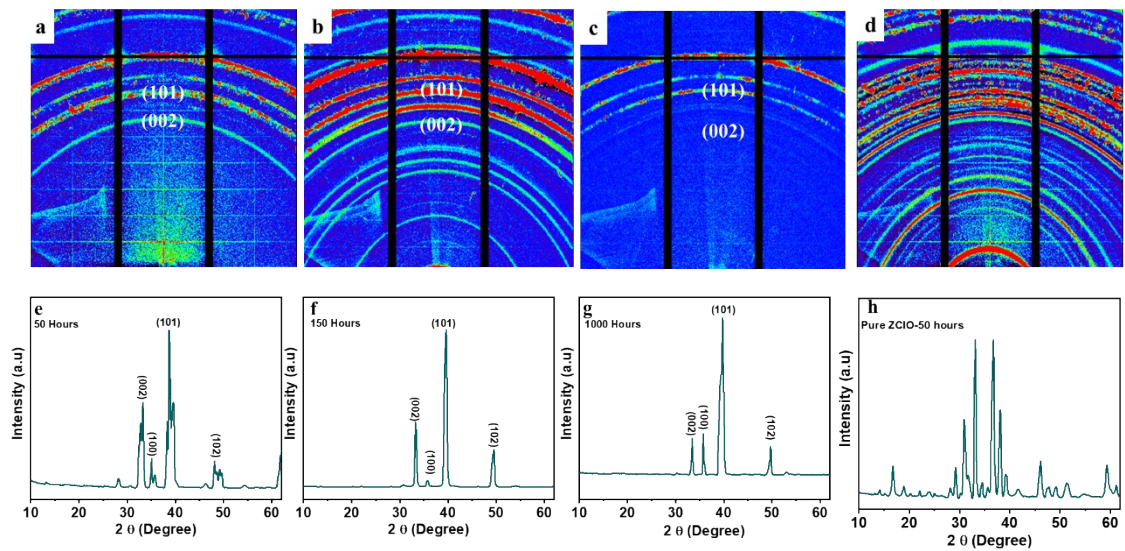
Figure S14. **a-c** GIXRD images obtained in the designed electrolyte after 50, 100, 500 cycles. **d** GIXRD images obtained in pure ZClO electrolyte. **e-g** 2θ integration in the designed electrolyte after 50, 100, 500 cycles. **h** 2θ integration in pure ZClO electrolyte
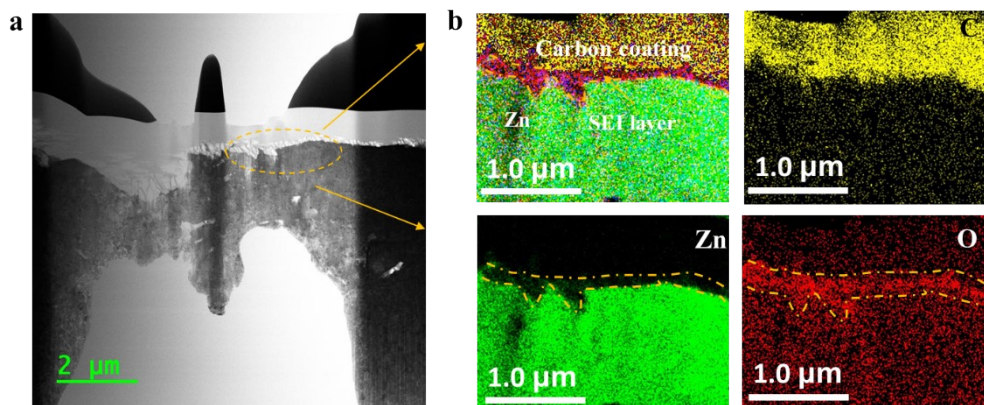
Figure S15 TEM mapping results of zinc cycled in designed electrolyte.
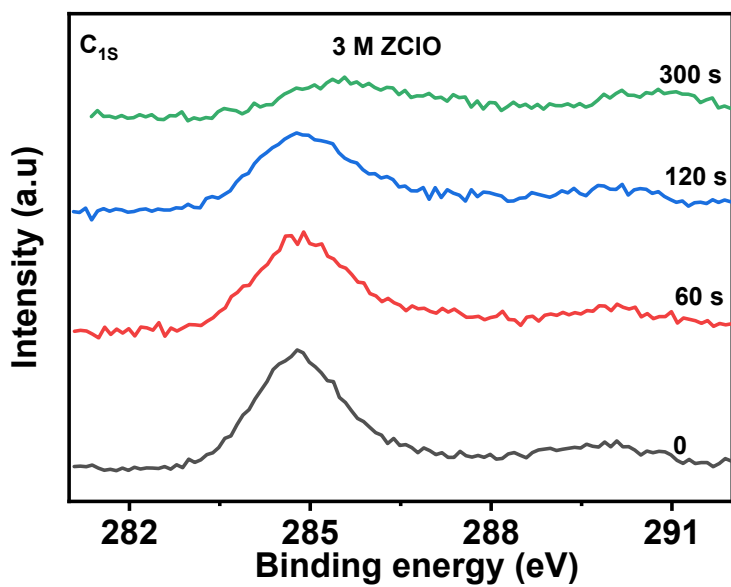
Figure S16. In-depth XPS of C_{1s} signal in 3.0 M ZClO.
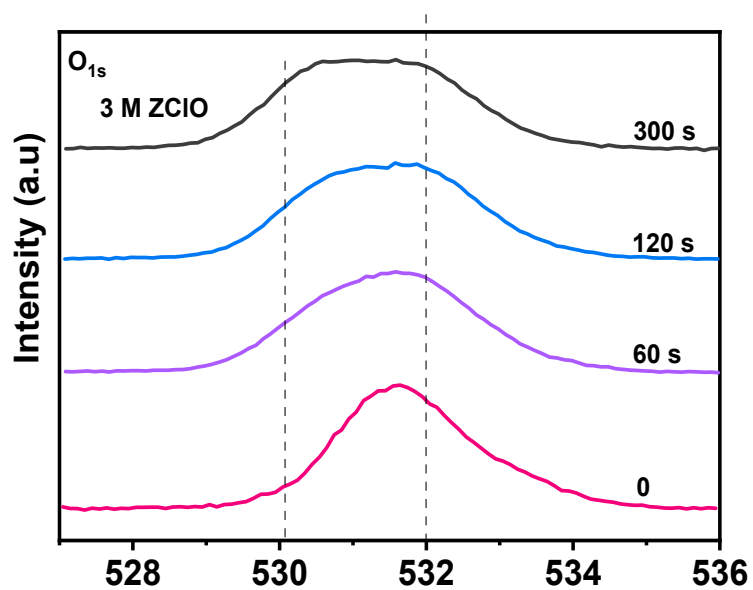
Figure S17. In-depth XPS of O_{1s} signal in 3.0 M ZClO.
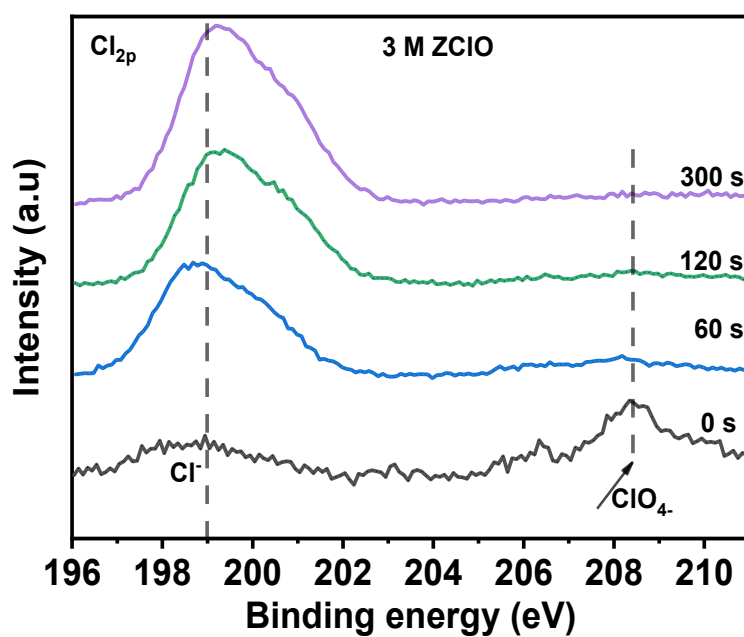
Figure S18. In-depth XPS of Cl_{2p} signal in 3.0 M ZClO.
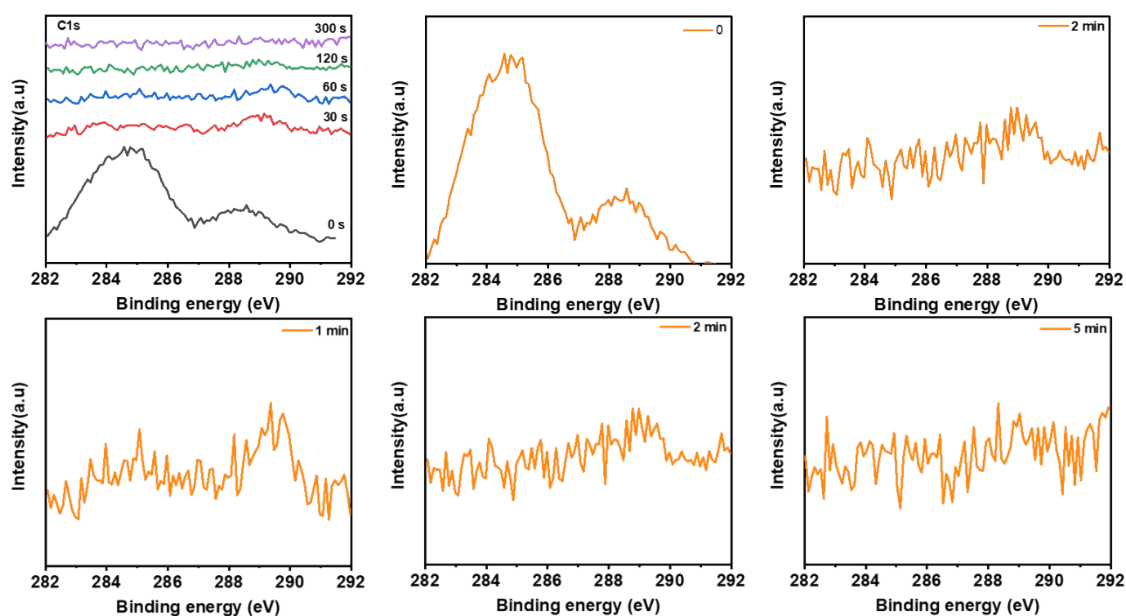
Figure S19 In-depth XPS of C_{1s} signal in 3.0 M ZClO-0.3 $Zn(OAc)_2$ electrolyte with pretreatment of CO_2 removal.
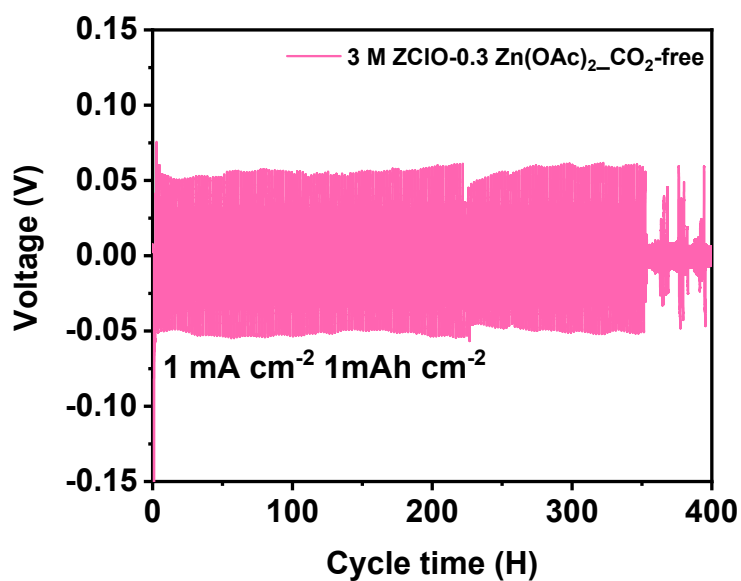
Figure S20. Long-term cycling performance of symmetric cell assembling in CO_2-free environments using designed electrolyte at 1 mA cm^{-2}.
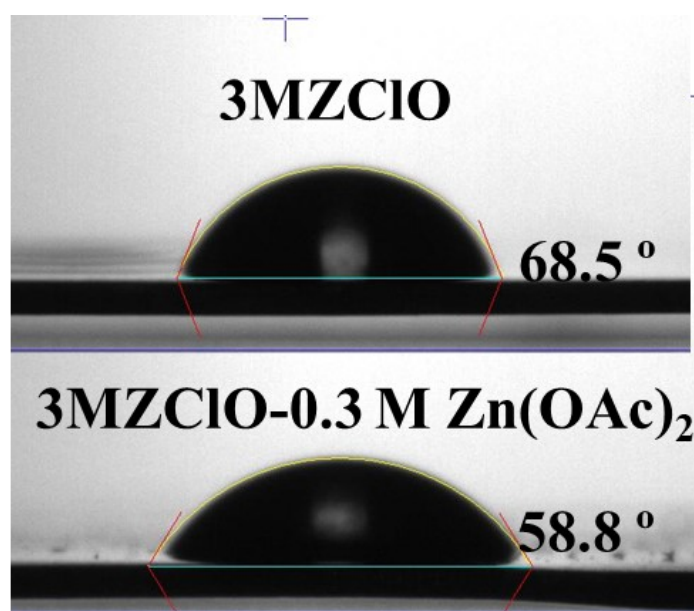
Figure S21. The contact angle of different electrolytes.

With 0.3 M Zn(OAc)$_2$ additive, the contact angle of the electrolytes decreases form 68.5 ° to 58.8°.
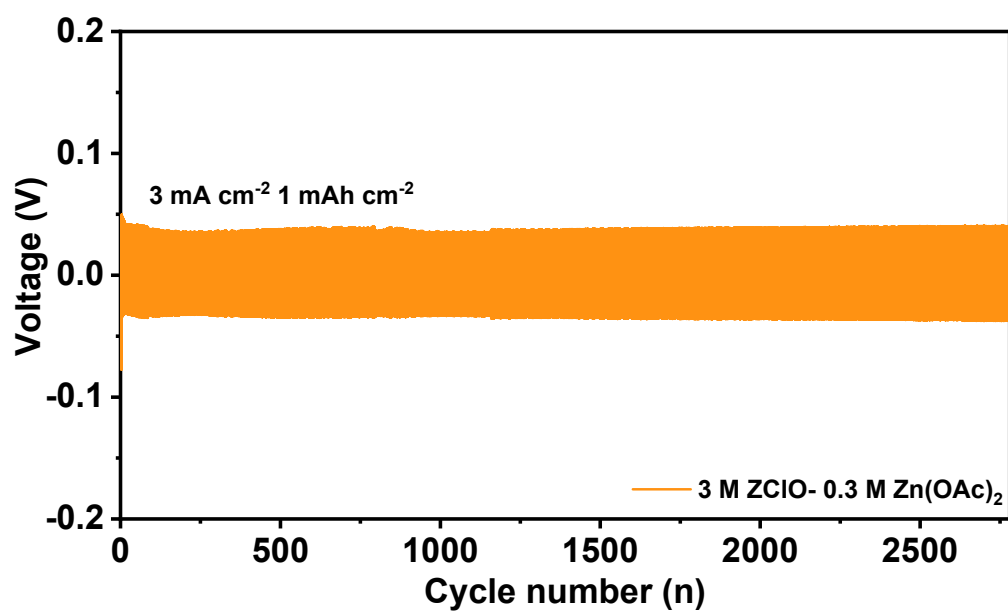
Figure S22. Long-term cycling performance of symmetric cell at 3 mA cm^{-2}.
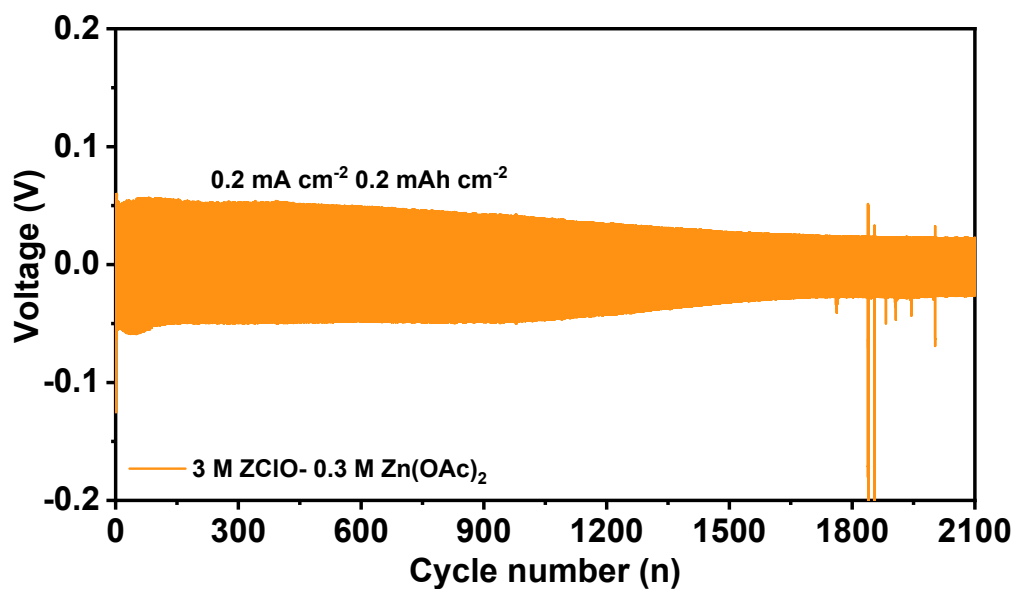
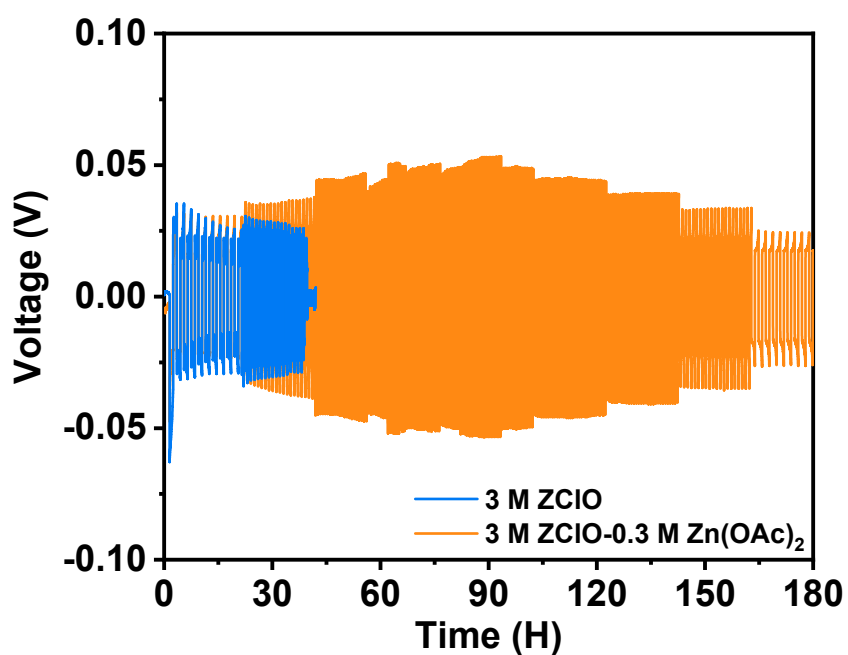Figure S23. Long-term cycling performance of symmetric cell at 0.2 mA cm^{-2}.

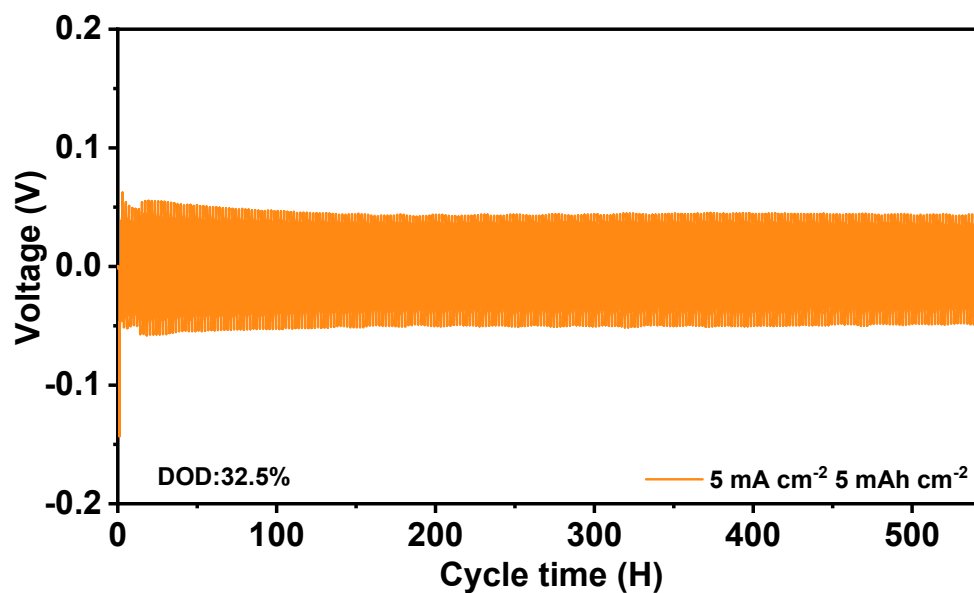Figure S24. Rate performance of symmetric cell using different electrolytes.

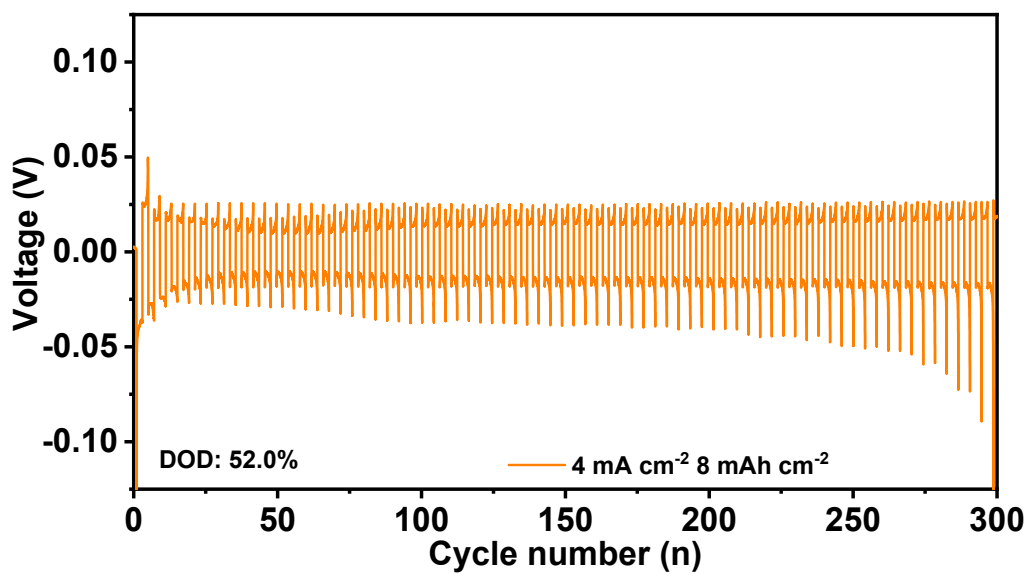Figure S25. Long cycling of the symmetric cell using designed electrolyte at a DOD of 32.5%.

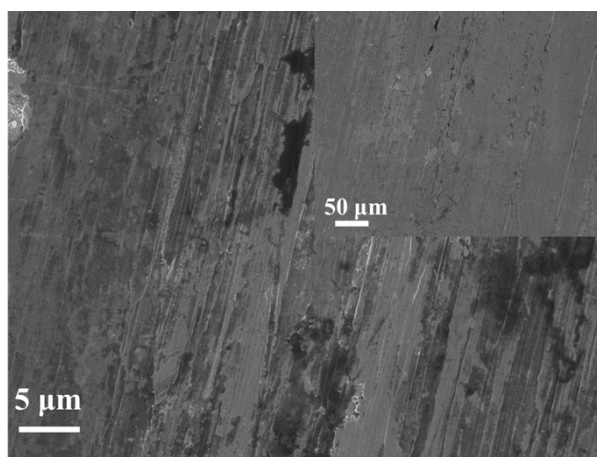Figure S26. Long cycling of the symmetric cell using designed electrolyte at a DOD of 52.0 %.

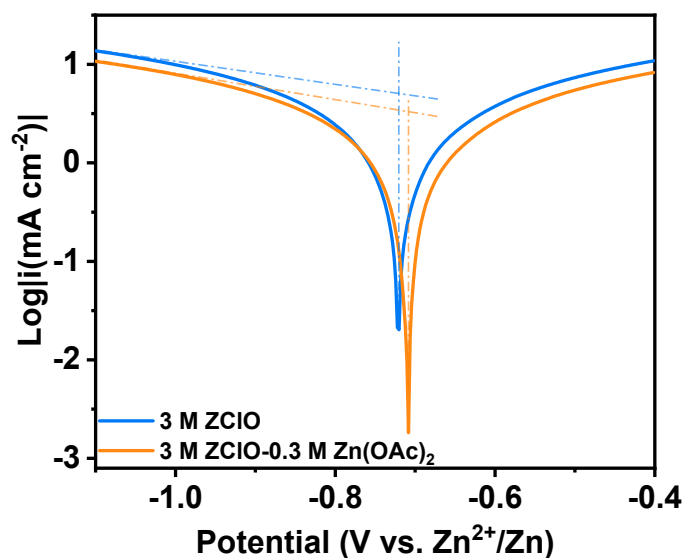Figure S27 The surface structure of the electrode before cycling

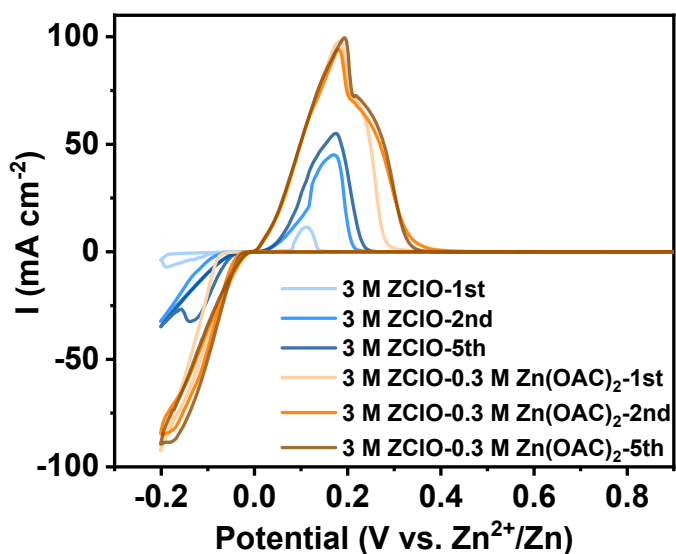Figure S28. Tafel plots of different electrolytes

Figure S29. CV curves in Zn||Cu cell with different electrolytes.

The side oxide peak should attributed to the oxidation of Cu, ($Cu(s) \rightarrow Cu^+ + e^-$, $E_0 = -0.52\ V\ vs.SHE/\ 0.24\ V\ vs\ Zn^{2+}/Zn$). When we replaced the Cu with stainless steel, the side oxidation peak was disappeared.
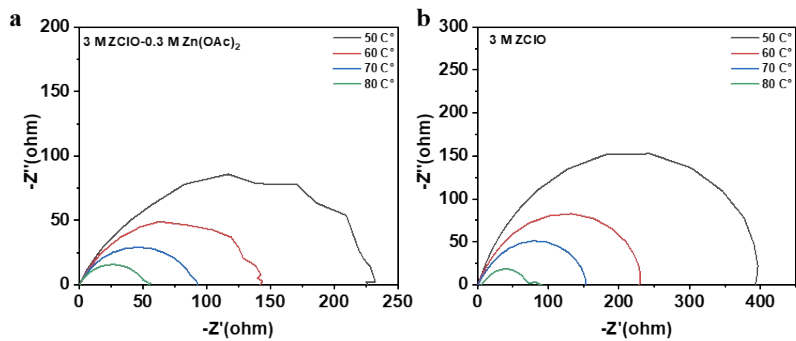
Figure S30. a-b EIS of symmetric cell in designed electrolyte (a) and pure ZClO electrolyte (b).
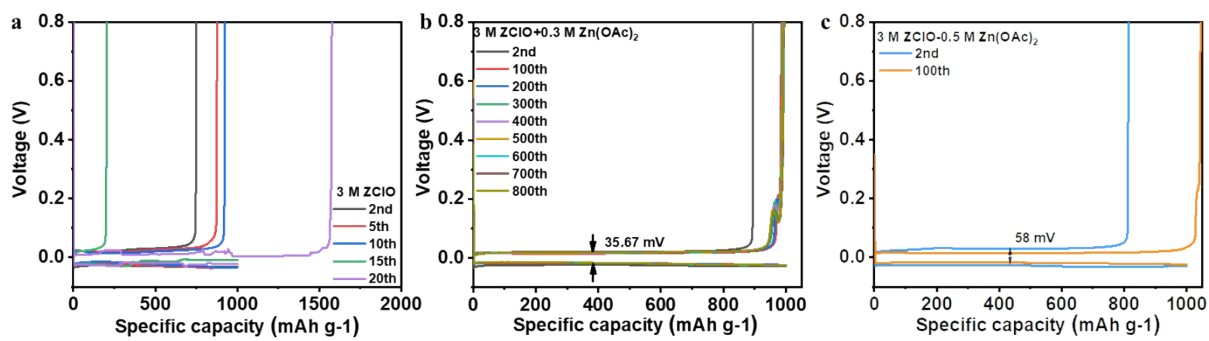

Figure S31. Voltage hysteresis of batteries using electrolytes with various Zn (OAc)$_2$ additive.
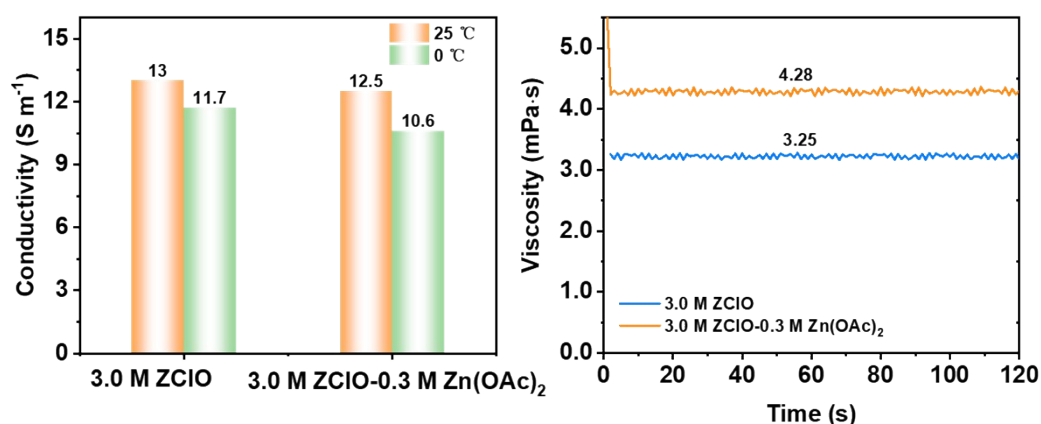
Figure S32. Comparison of ionic conductivity and viscosity of 3 M ZClO and 3 M ZClO-0.3 m $Zn(OAc)_2$ electrolytes.

With 0.3 M $Zn(OAc)_2$ additive, the ionic conductivity of the electrolyte decreases a bit compared with pure 3.0 ZClO electrolyte(13 S m^{-1} vs 11.7 S m^{-1} at 25 ℃ and 12.5 S m^{-1} vs 10.6 S m^{-1} at 0 ℃) due to the large size and slow movement of OAc$^-$ in electrolytes. The slightly higher viscosity is also observed with $Zn(OAc)_2$ additive may due to the strong interaction of OAc$^-$ with water.
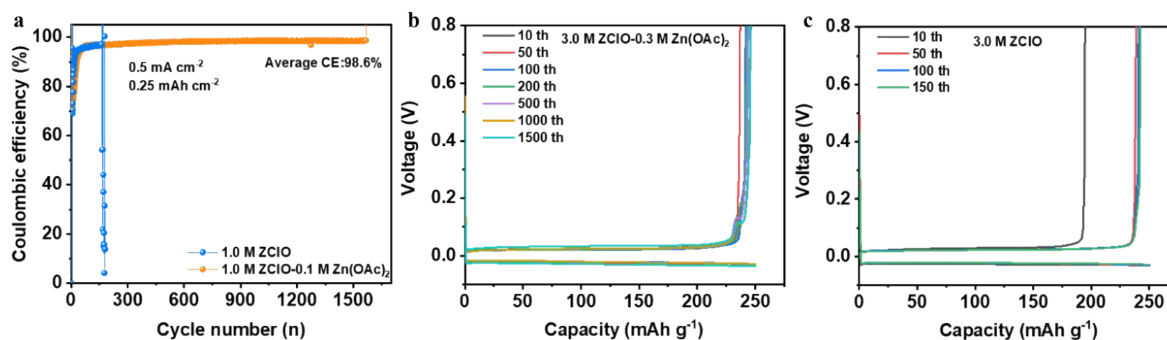

Figure S33. **a** Coulombic efficiency of Zn‖ Cu cells at 0.5 mA cm^{-2}. **b-c** Charge/discharge curves in (b) designed electrolyte and (c) 3 M ZClO electrolyte.
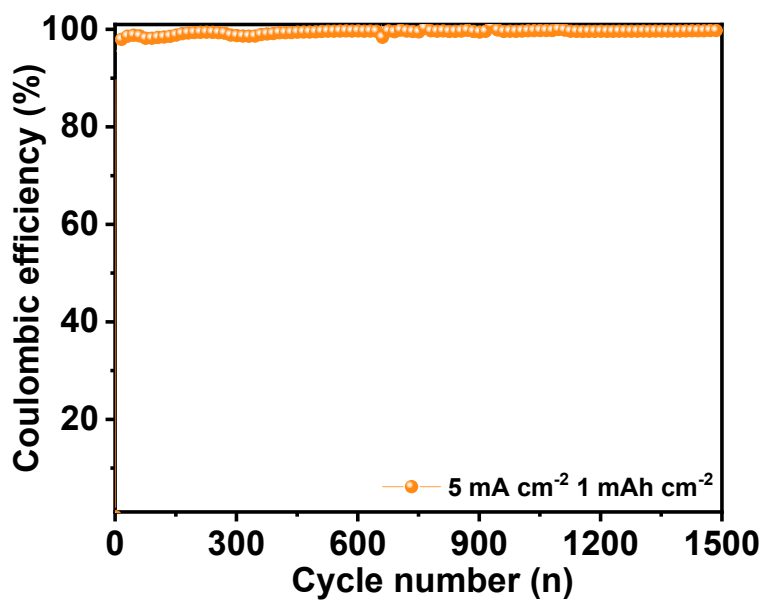
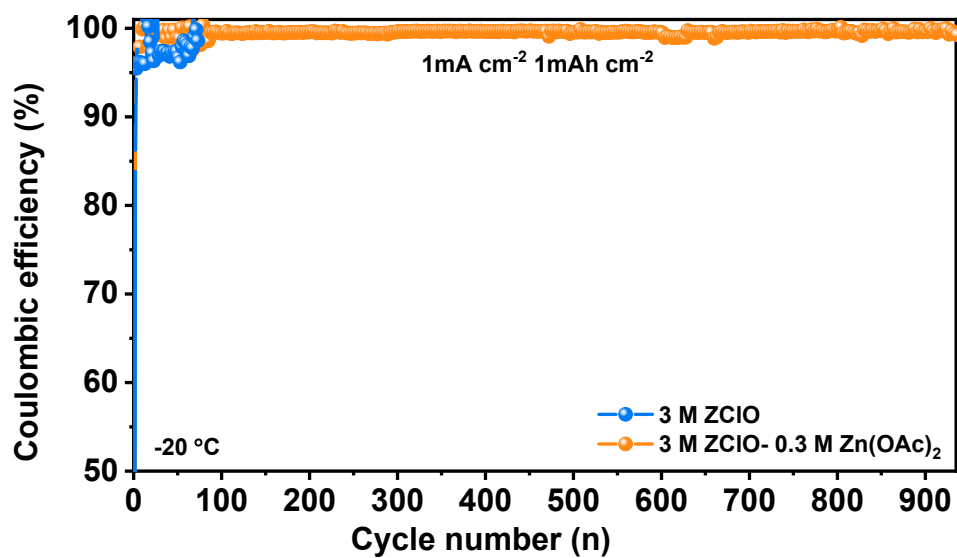Figure S34. Coulombic efficiency of battery employing designed electrolyte at 5.0 mA cm^{-2}.

Figure S35. Coulombic efficiency of battery employing designed electrolyte at -20 ºC.
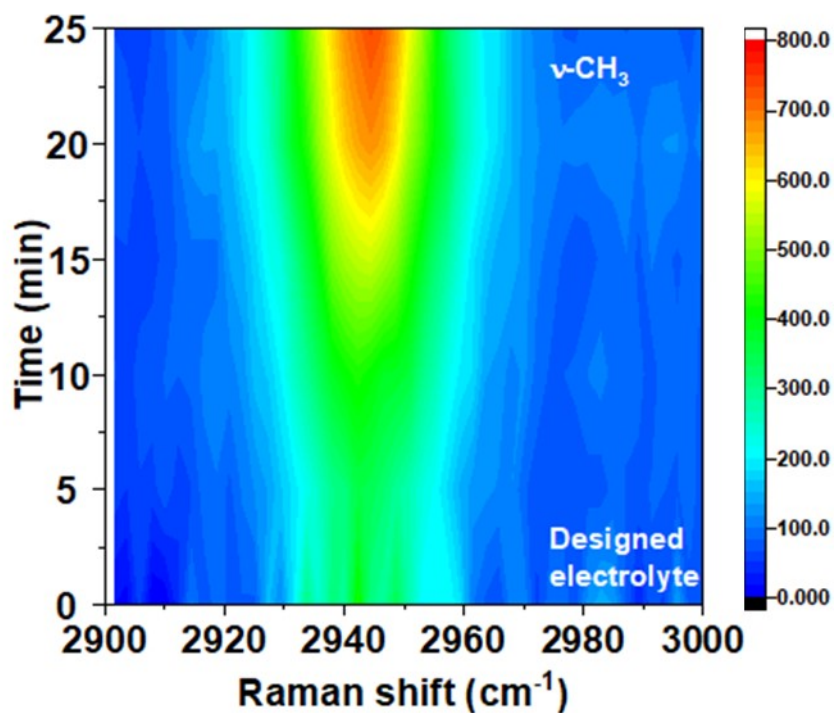
Figure S36 In-situ Raman results of electrode/electrolyte interface in 3 M ZClO-0.3 M Zn(OAc)$_2$ electrolyte.

Figure S37. EIS of Zn||I$_2$ full cell with various electrolyte
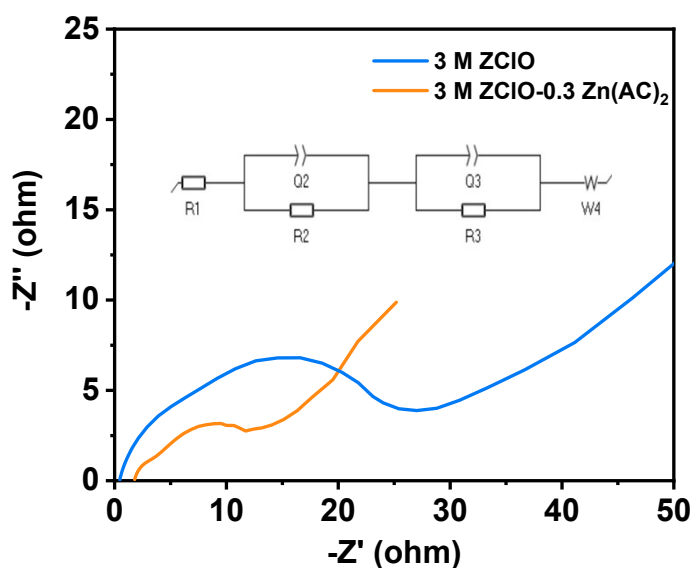
Both cells display two semicircles, which can be assigned to the charge transfer resistance (R_{ct}/R_2) in the mid-frequency region and the resistance associated with Zn^{2+} crossing SEI (R_{SEI}/R_3). R_1 represents the internal resistance.
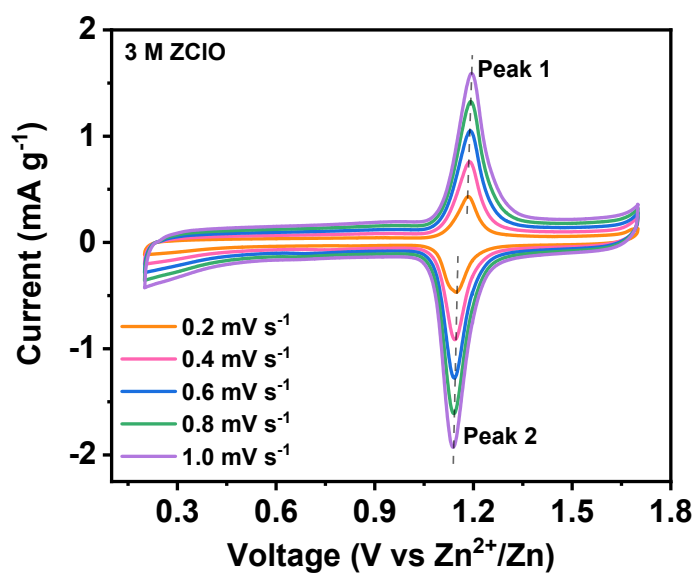
Figure S38. CV curves of battery with 3 M ZClO electrolyte
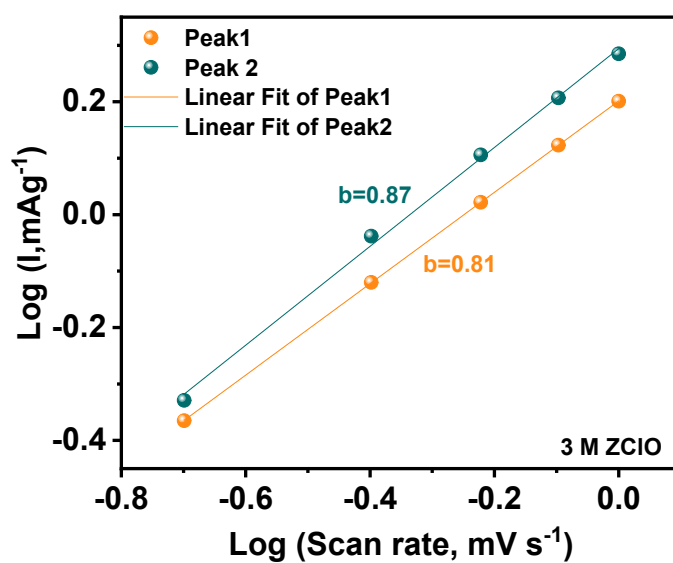
Figure S39. Fitted b values in 3 M ZClO electrolyte
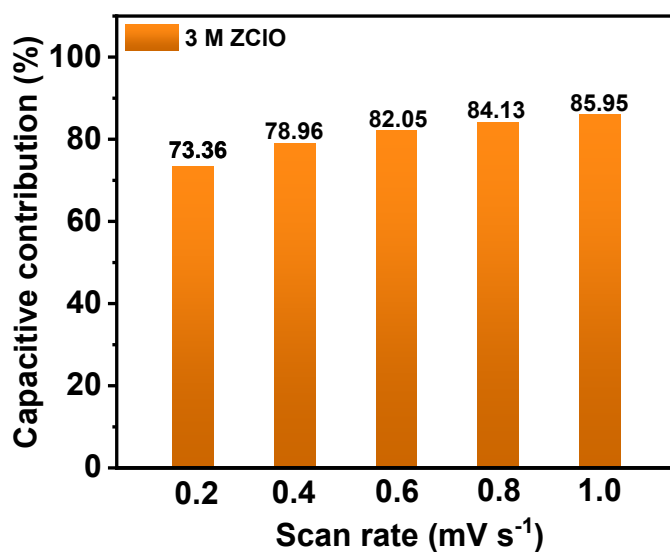
Figure S40. Capacitive contribution in 3 M ZClO electrolyte

The quantitative capacitive contributions were then calculated by the equation $i=k_1 v+k_2 v^{1/2}$, in which $k_1 v$ and $k_2 v^{1/2}$ represent the capacity contribution made by capacitive and ionic diffusion behavior, respectively.

Figure S41. Raman spectra (CH_3 signal) of electrolytes (DE represents designed electrolytes) with different amounts of I_3^- additives
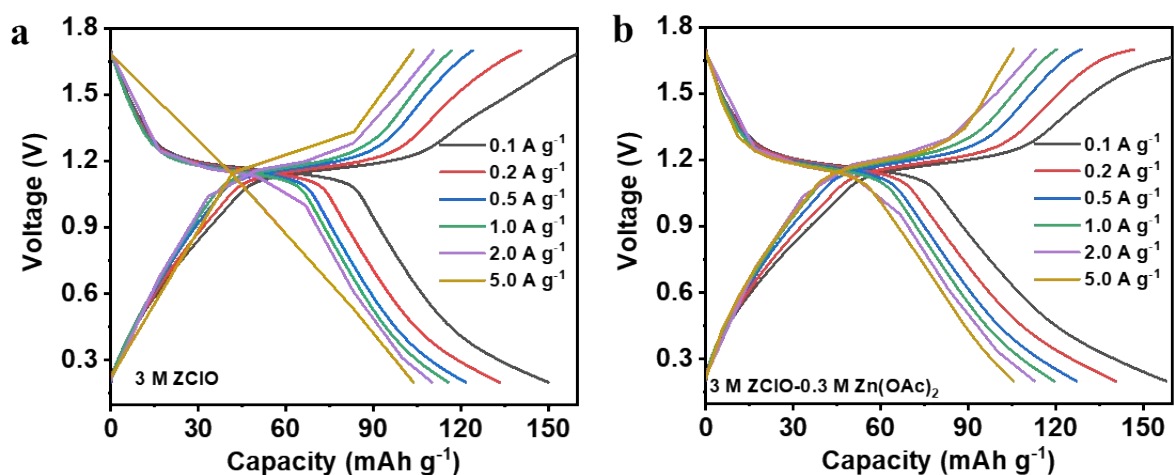
Figure S42. Charge and discharge curves of Zn||I_2/AC with different electrolyte at 25 ºC.

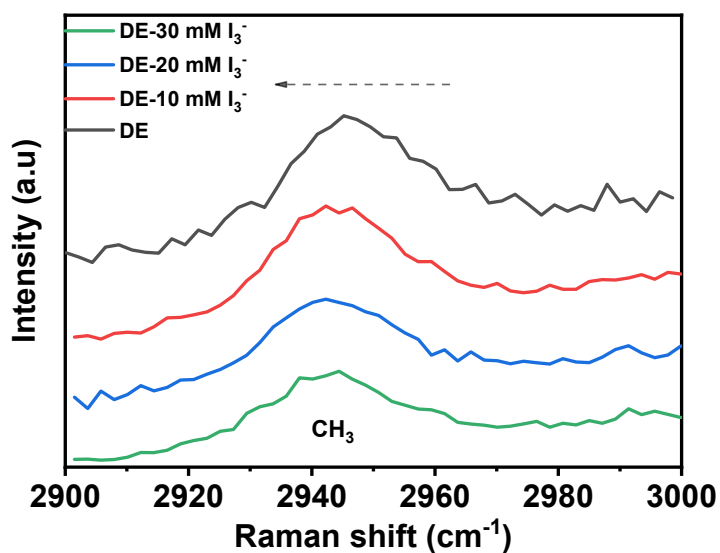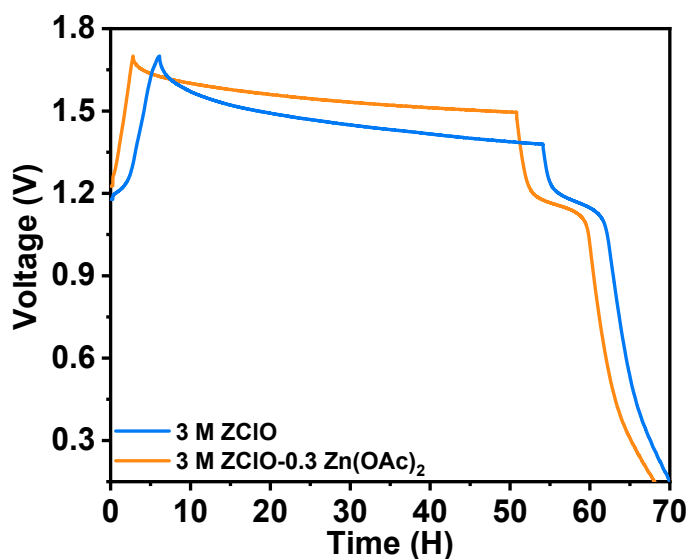Figure S43. Self-discharge curves of Zn||I_2/AC in different electrolytes at 25 ºC.

The self-discharge tests of Zn|| I_2/AC full cells were conducted at room temperature. After five cycles at 0.1 A g^{-1}, the Zn|| I_2/AC full cell was fully charged to 1.7 V, then rested at open circuit voltage (OCV) for 2 days (48 h) to monitor the decay of OCV of the cell. After 48 hours of resting, the full cell using the designed electrolyte exhibits a higher potential of 1.5 V (vs. Zn^{2+}/Zn), contrasting with 1.38 V in pure ZClO electrolytes, proving the inhibited dissolution of cathode materials with the presence of $Zn(OAc)_2$ additive.
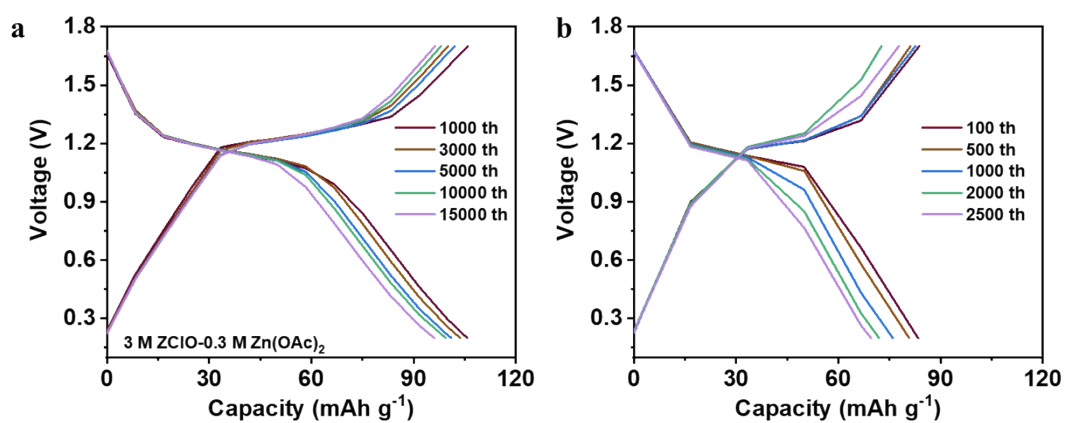
Figure S44. Charge and discharge curves of Zn||I$_2$/AC with different electrolytes at -40 ºC.
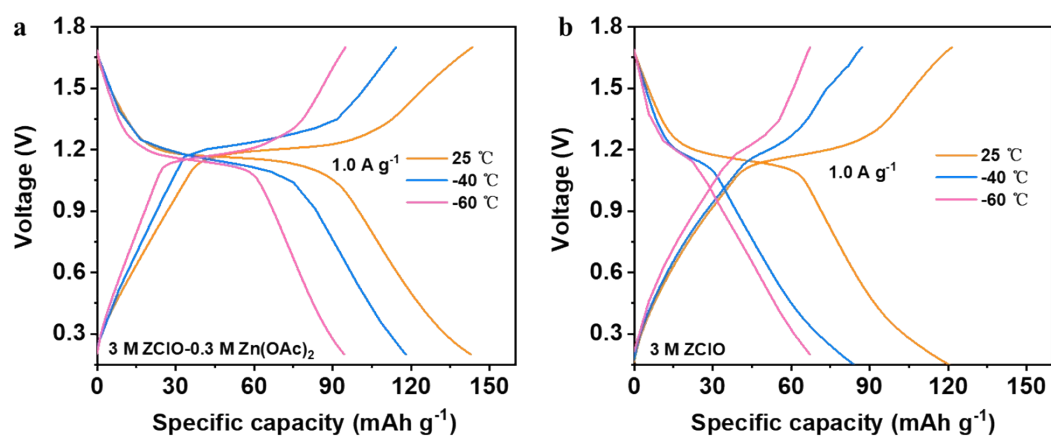
Figure S45. Charge and discharge curves of Zn||I$_2$/AC with different electrolytes at varying temperatures
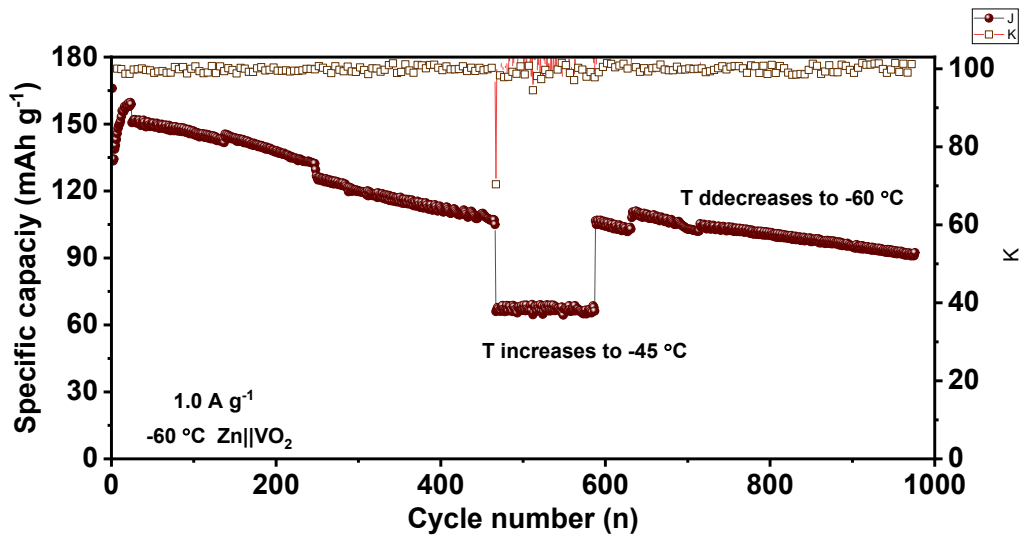
Figure S46. Long-term cycling performance of Zn‖ VO$_2$ at 1.0 A g-1 at -60 ºC.
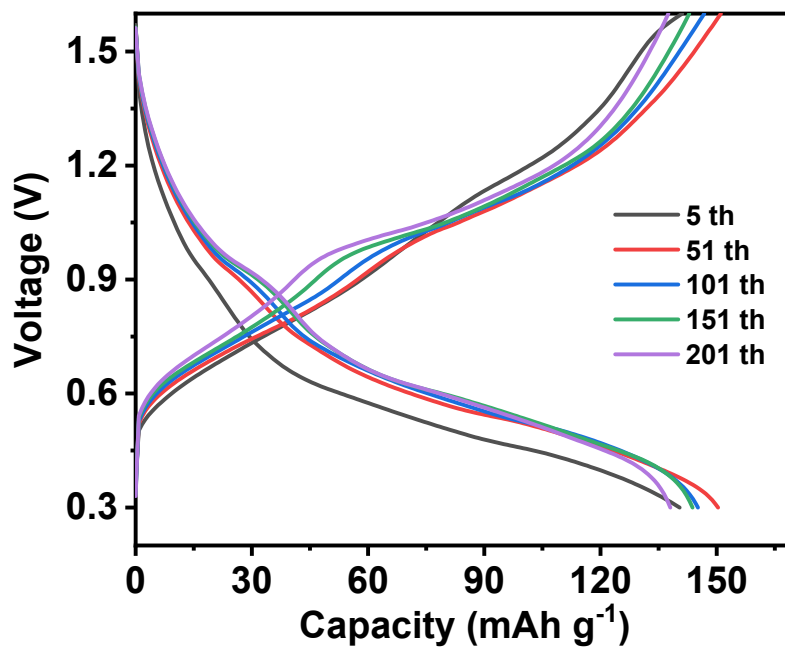
Figure S47. Charge and discharge curves of Zn‖VO$_2$ with designed electrolyte at -60 ºC.
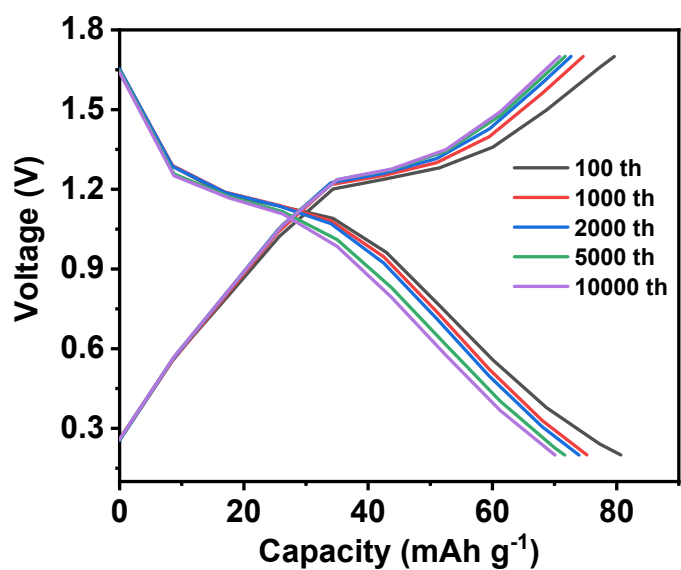
Figure S48. Charge and discharge curves of Zn||I$_2$/AC pouch cell at -40 ºC.
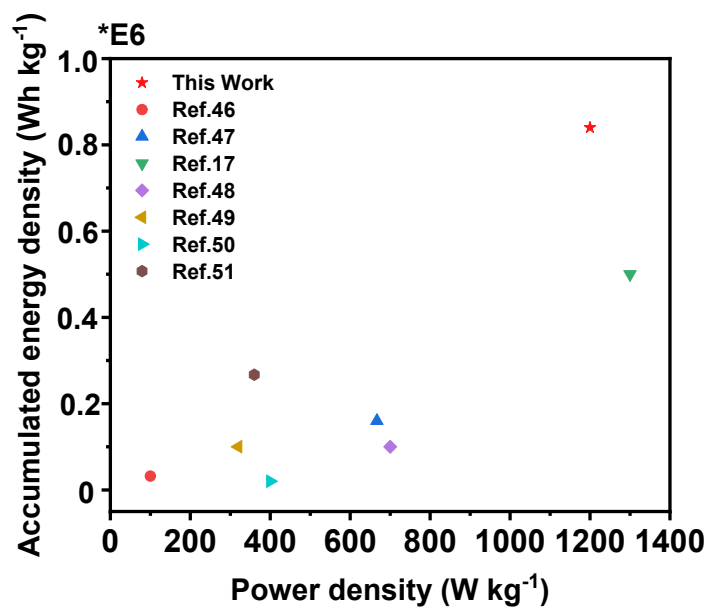
Figure S49 Ragone plots of Zn||I$_2$/AC pouch cells compared with previously reported ZIBs.
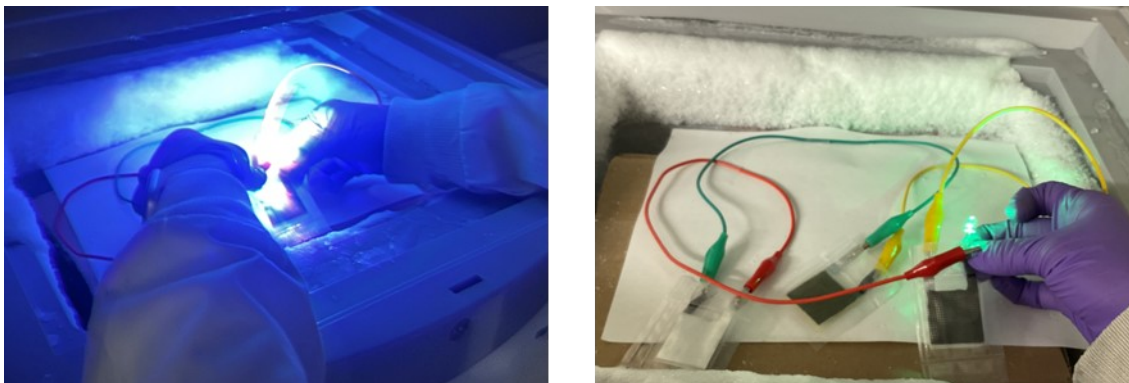
Figure S50. Three Pouch cells connected in series powering an LED light
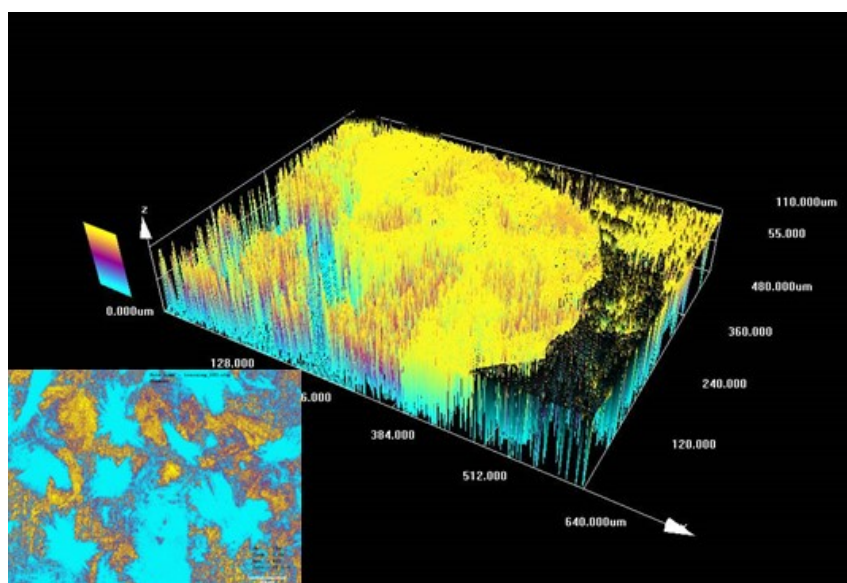
Figure S51. 2D and 3D confocal microscope image of zinc cycled in pure ZClO electrolyte in Zn||I$_2$/AC full cell.
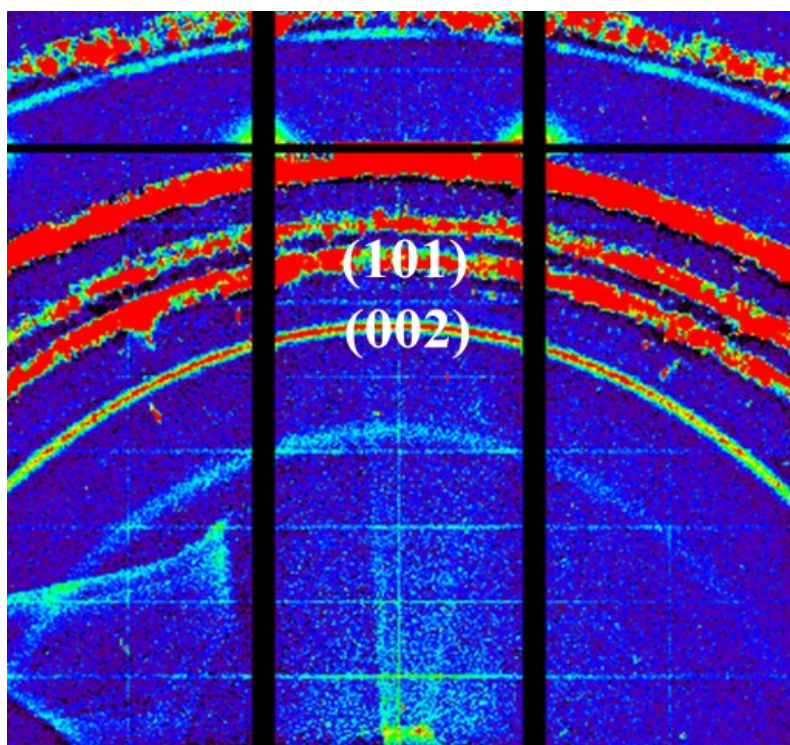
Figure S52. 2D XRD of zinc cycled in designed electrolyte in Zn||I$_2$/AC full cell.
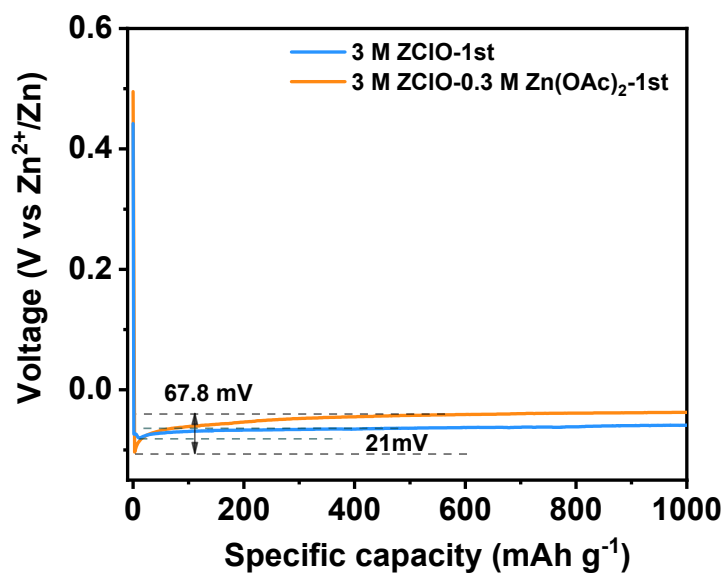
Figure S53. Nucleation overpotential in different electrolytes (Zn||Cu cell).
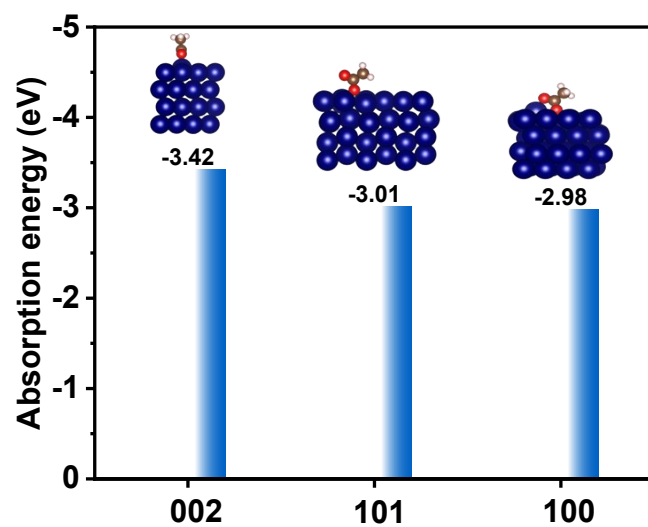
Figure S54. Absorption energy of OAc⁻ on different Zn plane.
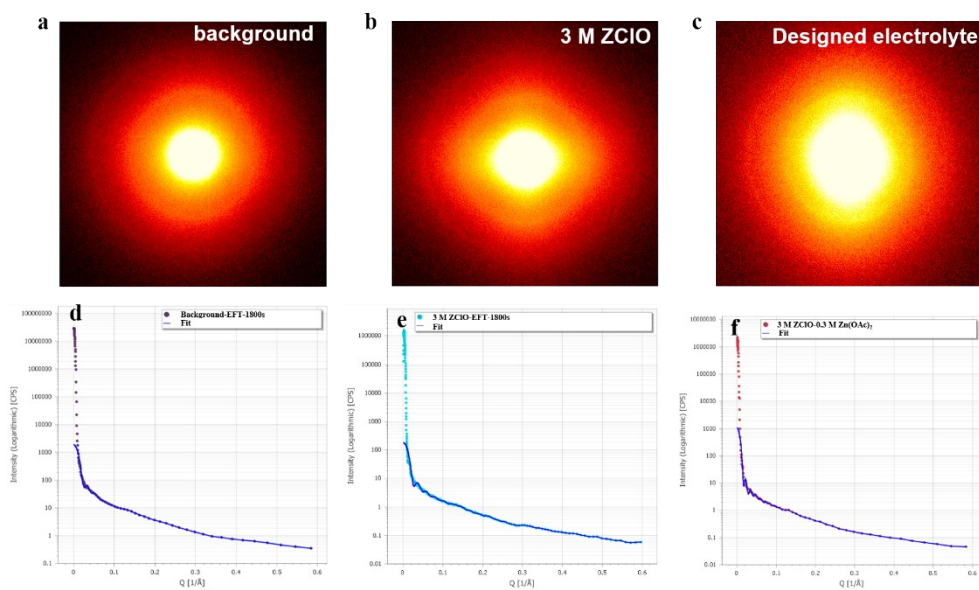
Figure S55 a 2D of scattering information of background (carbon cloth). b, c 2D of scattering information of zinc deposited in different electrolyte. d-f SAXS intensity profiles for different electrolytes.
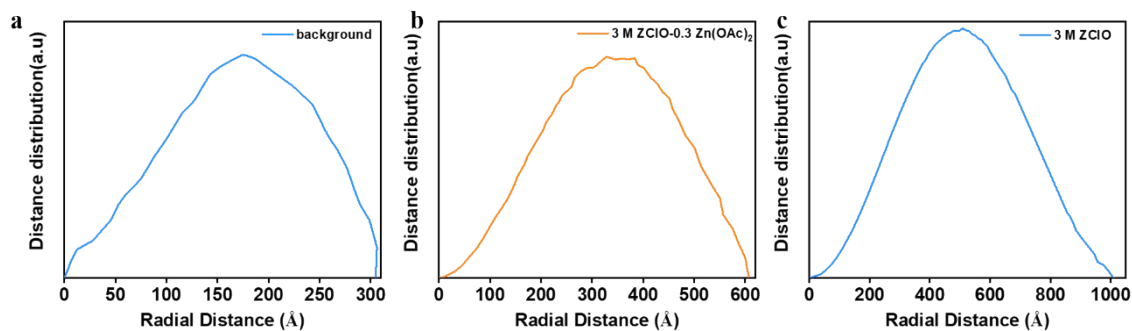
Figure S56 SAXS profile showing the radius size.
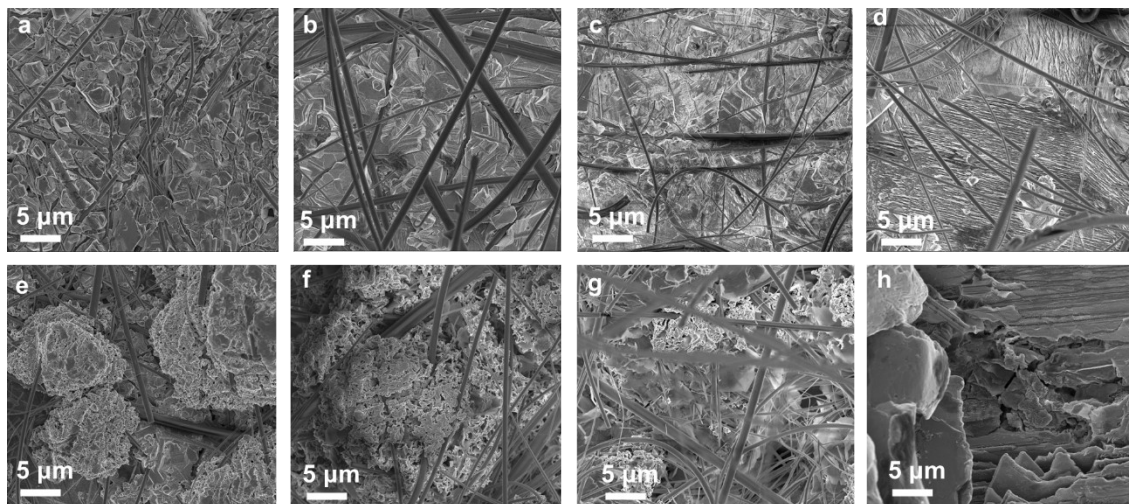
Figure S57 SEM images of Zn plating at 1mA cm^{-1} for 1h. (a-d) In 3.0 M ZClO-0.3 M Zn(OAc)$_2$ for 1st plating (a), 2nd plating (b), 5th plating (c), 10th plating (d). (e-h) In 3.0 M ZClO for 1st plating (e), 2nd plating (f), 5th plating (g), 10th plating (h).

3. Discussions

1. Investigation of 101 deposition mechanisms

The preferred orientation is the result of the contribution of surface energy and work function of the crystallographic planes. Surface energy primarily governs the nucleation process, while the work function impacts the growth patterns of zinc deposits [9]. Planes with lower surface energy and higher work function (associated with nucleation overpotential) are more likely to promote the formation of planes with lower atomic density. Among the crystallographic planes, the basal plane (002) exhibits the highest atomic packing density, while the prismatic plane (100) has the lowest. The (101) plane falls between these two in terms of atomic packing density. For the designed system, the surface energy, as reflected by the contact angle (**Figure S21**), is lower than that obtained in pure ZClO electrolyte while the nucleation overpotential is higher (**Figure S53**). These properties favor vertical zinc deposition over horizontal growth. Additionally, the affordable orientations are determined by the growth rate of various crystallographic planes, which are influenced by the interaction of additives with the growing surface [10]. The DFT calculations demonstrate the OAc^- exhibits the lowest absorption energy on the (002) plane (-3.42 eV), indicating a strong tendency to adsorb on the zinc surface. This adsorption effectively blocks the (002) facets, promoting vertical growth of zinc electrodeposits by inhibiting lateral expansion along the basal plane [11] (**Figure S54**).

The nucleation patterns and morphological evolution of zinc in various electrolytes were further investigated using ex-situ small-angle X-ray scattering (SAXS) techniques and SEM imaging. Based on classical nucleation theory, the size of nuclei decreases as the overpotential increases, while the areal nuclei density increases with the cube of the overpotential for spherical nuclei [12]. The formation of smaller nuclei and a higher nuclei density promotes a more compact deposition morphology. To investigate the effect of OAc^- on zinc nucleation, ex-situ SAXS measurements were conducted. The results reveal that in the presence of the OAc^- additive, the nuclei formed in the designed electrolyte had an average size of 350 Å, which is smaller compared to those formed in the pure $Zn (ClO_4)_2$ (ZClO) electrolyte (500 Å) (**Figure S55 and Figure S56**). SEM images show that during the first and second cycles, zinc deposited in the designed electrolyte exhibits a dense and randomly oriented morphology, whereas zinc cycled in the pure ZClO electrolyte forms a loose, sponge-like structure. Extending the cycling to 5

and 10 cycles, the dense, vertically oriented zinc deposition predominates in the designed electrolyte, in contrast to the formation of large flakes in the pure ZClO electrolyte (**Figure S57)**. Considering the SEI formation takes time, as evidenced by the gradual CE increases in **Figure S8**, we attribute the homoepitaxial growth of zinc to the dynamic adsorption of OAc$^-$. In conclusion, the reduced surface energy and increased nucleation overpotential in the designed electrolyte facilitate the formation of smaller zinc nuclei with higher areal density. The dynamic adsorption of OAc$^-$ on the (002) plane and the high nucleation overpotential further directs zinc deposition preferentially in the vertical direction, particularly along the (101) plane, rather than facilitating horizontal growth.

4. Supporting Tables

Supplementary Table 1. Price of zinc salts (Referred sigma-Aldrich)

Salts	Price/kg
$ZnCl_2$	308 CAD
$ZnSO_4$	274 CAD
$Zn(ClO_4)_2$	324 CAD
$Zn(OTF)_2$	6740 CAD

Supplementary Table2. The coordination environment of Zn^{2+} in ZClO electrolytes

Salts	$Zn-O(ClO_4^-)$	$Zn-O (H_2O)$	$Zn-O(OAc^-)$
1.0 M ZClO	0.195	5.803	
2.0 M ZClO	0.576	5.432	
3.0 M ZClO	1.043	4.999	
3.5 M ZClO	1.304	4.786	
Designed system	0.890	4.789	0.321

Supplementary Table3. Fitting results of EIS

curves in Figure S30 System	R_1	R_2	R_3
3.0 M ZClO	0.42 Ω	4.33 Ω	21.36 Ω
3.0M ZClO-0.3 M $Zn(OAc)_2$	1.55 Ω	3.76 Ω	7.61Ω

5. References

[1] Chen Y, Gong F, Deng W, et al. Dual-function electrolyte additive enabling simultaneous electrode interface and coordination environment regulation for zinc-ion batteries[J]. Energy Storage Materials, 2023, 58: 20-29.

[2] Deng W, Xu Z, Li G, et al. Self-Transformation Strategy Toward Vanadium Dioxide Cathode For Advanced Aqueous Zinc Batteries[J]. Small, 2023: 2207754.

[3] B. Ravel and M. Newville, ATHENA, ARTEMIS, HEPHAESTUS: data analysis for X-ray absorption spectroscopy using IFEFFIT, Journal of Synchrotron Radiation 12, 537–541 (2005) doi:10.1107/S0909049505012719

[4] Funke, H.; Scheinost, A. C.; Chukalina, M. Wavelet analysis of extended X-ray absorption fine structure data.*Physical Review* 2005, B 71, 094110.

[5] D. Joubert, Phys Rev B Condens Matter Mater Phys 1999, 59, 1758. https://doi.org/10.1103/PhysRevB.59.1758.

[6] Abraham, M. J., Murtola, T., Schulz, R., Páll, S., Smith, J. C., Hess, B., & Lindah, E. (2015). Gromacs: High performance molecular simulations through multi-level parallelism from laptops to supercomputers. SoftwareX, 1–2, 19–25. https://doi.org/10.1016/j.softx.2015.06.001.

[7] Xu, Z., Li, M., Sun, W., Tang, T., Lu, J., & Wang, X. (2022). An Ultrafast, Durable, and High-Loading Polymer Anode for Aqueous Zinc-Ion Batteries and Supercapacitors. Advanced Materials, 34(23). https://doi.org/10.1002/adma.202200077

[8] Qiu, M., Sun, P., Han, K., Pang, Z., Du, J., Li, J., ... & Mai, W. (2023). Tailoring water structure with high-tetrahedral-entropy for antifreezing electrolytes and energy storage at− 80° C. *Nature Communications*, *14*(1), 601.

[9] Szeptycka, B. "Effects of organic compounds on the electrocrystallization of nickel." Russian journal of electrochemistry 37 (2001): 684-689.

[10] Sato, Ryoitiro. "Crystal growth of electrodeposited zinc: an electron diffraction and electron microscopic study." Journal of The Electrochemical Society 106.3 (1959): 206.

[11] Zhang, Weidong, et al. "Dynamic interphase–mediated assembly for deep cycling metal batteries." Science Advances 7.49 (2021): eabl3752.

[12] Pei, Allen, et al. "Nanoscale nucleation and growth of electrodeposited lithium metal." *Nano letters* 17.2 (2017): 1132-1139.